Heat capacity of hydrous trachybasalt from Mt Etna: comparison with CaAl2Si2O8 (An)–CaMgSi2O6 (Di) as basaltic proxy compositions

DOI:10.1007/s00410-015-1196-6

Contributions to Mineralogy and Petrology

Heat capacity of hydrous trachybasalt from Mt Etna: comparison with CaAl2Si2O8 (An) - CaMgSi2O6 (Di) as basaltic proxy compositions

--Manuscript Draft--

Manuscript Number:	CTMP-D-15-00019R1
Full Title:	Heat capacity of hydrous trachybasalt from Mt Etna: comparison with CaAl2Si2O8 (An) - CaMgSi2O6 (Di) as basaltic proxy compositions
Article Type:	Original Paper
Keywords:	specific heat, viscosity, thermochemical and transport properties, hydrous Etna trachybasalt, anorthite-diopside-water system
Corresponding Author:	Daniele Giordano, Faculty (Research position) Universita degli Studi di Torino Torino, ITALY
Corresponding Author Secondary Information:	
Corresponding Author's Institution:	Universita degli Studi di Torino
Corresponding Author's Secondary Institution:	
First Author:	Daniele Giordano, Faculty (Research position)
First Author Secondary Information:	
Order of Authors:	Daniele Giordano, Faculty (Research position)
	Alex Rober Nichols, PhD
	Marcel Potuzak, PhD
	Danilo Di Genova, PhD
	Claudia Romano, Faculty (associate professor)
	James Kelly Russell, Faculty (full professor)
Order of Authors Secondary Information:	
Funding Information:	
Abstract:	The specific heat capacity (Cp) of six variably-hydrated (~ 3.5 wt% H2O) iron-bearing Etna trachybasaltic glasses and liquids has been measured using differential scanning calorimetry from room temperature across the glass transition region. These data are compared to heat capacity measurements on thirteen melt compositions in the iron-free anorthite (An) - diopside (Di) system over a similar range of H2O contents. These data extend considerably the published Cp measurements for hydrous melts and glasses. The results for the Etna trachybasalts show non-linear variations in, both, the heat capacity of the glass at the onset of the glass transition (i.e. Cpg) and the fully relaxed liquid (i.e. Cpl) with increasing H2O content. Similarly, the "configurational heat capacity" (i.e. Cpc = Cpl - Cpg) varies non-linearly with H2O content. The An-Di hydrous compositions investigated show similar trends, with Cp values varying as a function of melt composition and H2O content. The results show that values in hydrous Cpg, Cpl and Cpc in the depolymerized glasses and liquids are substantially different from those observed for more polymerized hydrous albitic, leucogranitic, trachytic and phonolitic multicomponent compositions previously investigated by Bouhifd et al. (2006). Polymerized melts have lower Cpl, Cpc and higher Cpg with respect to more depolymerized compositions. The covariation between Cp values and the degree of polymerization in glasses and melts is well described in terms of a modified SMhydrous, and NBO/Thydrous. Values of Cpc increase sharply with increasing depolymerization up to SMhydrous ~30-35 mol % (NBO/Thydrous ~ 0.5) then decrease to an almost constant value. The partial molar heat capacity of H2O for both glasses (CpgH2O) and liquids

	($CplH_2O$) appears to be independent of composition and, assuming ideal mixing, we obtain a value for $CplH_2O$ of 79 J mol-1 K-1. However, we note that a range of values for $CplH_2O$ (i.e. ~ 78 - 87 J mol-1 K-1) proposed by previous workers will reproduce the extended data to within experimental uncertainty. Our analysis suggests that more data are required in order to ascribe a compositional dependence (i.e. non-ideal mixing) to $CplH_2O$.
Response to Reviewers:	Reply to comments/suggestions/additions REVIEWER 1 1. Sample description. The reviewer is interested in knowing more about the effect of iron species on structure and how this would affect the calculation of SM parameters. Here is a more detailed explanation of the reasons why we considered treating half of the total iron as a network former and other half as a network modifier in order to calculate the SM parameters. Iron speciation of hydrous samples was not measured in this paper and the assumed role of iron and water species is described in paragraph 3.2 (line 221 - 233 of the original manuscript).Di Muro et al. (2009) showed that basalts demonstrate that the sensitivity of glass structure to changing redox conditions decreases with increasing depolymerization. Mercier et al. (2009, 2010), based on a large number of measurements on various compositions, showed that water (i.e. hydrous melts) has a depolymerizing effect that seems to be independent from that of the other modifying components. Similarly it has been demonstrated by Giordano et al. (2008b) that the role of water on the structure is somehow independent from that of the other cations. However, in rare cases, such as for basaltic compositions it could also slightly increase the polymerization of the structure (Giordano et al., 2009b GCA). In order to know the exact role of the effective network modifiers and the role of iron species in the network structure further extensive research is required. This is not the objective and beyond the scope of this study. In particular, for hydrous melts this work would require much more than the just accurate measurements of iron partitioning. Even in anhydrous melts the effective partitioning of Fe and the structural role of Fe species is still poorly known (both Fe^{2+} and Fe^{3+} can have network former (coordination IV) and network modifier (coordination VI) or intermediate (coordination V) roles depending on the compositions). The role of iron in hydrous melts is even more complicated and has only been discussed in a few papers (e.g., Mercier et al., 2009; 2010 and Di Muro et al., 2009). Mercier et al., (2009; 2010) and Di Muro et al. (2009) use the same basaltic composition as that used here and are based on large sample statistics. They show that our decision of assuming iron as partitioned half as a FeO and half as Fe_2O_3 is the best choice we can make so far. Based on the data currently available, the SMhydrous parameter is the best estimation that can be made at present. Di Muro et al. (2009) is now referred to in the manuscript where readers can find the evaluation and the significance of the uncertainty of the calculated SM/SMhydrous parameters. On the basis of what is mentioned above, I believe that the role of iron species on anhydrous and hydrous basaltic glasses would have no significant effect in the structure nor in the calculation of the SM parameter. 2. We have added a small paragraph and two figures (as supporting online material) to describe the procedure used to perform the sensitivity calibration and calculate measurement accuracy. 3. The selected cooling/heating rate that we used for the calculation is, as reported at line 157 of the original manuscript, 10 K/min. 4. We changed it and, in order to be clearer about the role of pressure on the samples synthesized at high pressure, we have re-phrased that part of the paragraph, from line 149 to 158 of the new manuscript version. 5. These are the ways of expressing the same meaning, but we are happy to use the terms suggested by the reviewer. It has been modified throughout. 6. Corrected. 7. Corrected, we have changed it to match the journal style that requires J mol-1 K-1 to

be used.

8. Done

9. Done

10. The way how both NBO/T and SM parameters are calculated is explained on lines 221-233 of the original manuscript, as following:

Lines 224 to 226 state: " The modified SM parameter, referred to hereafter as SMhydrous, is calculated, in mol%, as the sum of the network modifier oxides plus the amount of dissolved H2O (Giordano et al. 2009; Mercier et al. 2009), without accounting for H2O speciation."

Lines 227 to 232 state: "Both the SMhydrous and NBO/Thydrous are considered to be representative of the degree of polymerization of the hydrous liquids (Mysen, 1988; Giordano et al. 2009) and both of them were calculated assuming, according to Mercier et al. (2009) and Di Muro et al. (2009) that half of the FeOtot (in wt%) partitions as FeO and the other half as Fe2O3, that implies a nearly constant [Fe2O3/(FeO + Fe2O3)] mass ratio value of about 0.5."

11. As explained above in reply to point one and discussed by Di Muro et al. (2009) - also referred to in the original manuscript iron speciation is not expected to significantly effect the structure of melts. As a consequence the effect of pressure will be not important. In addition, all samples are thermally re-equilibrated at atmospheric conditions during the first heating state and the pressure and thermal history undergone during hydrothermal syntheses will have even less of an effect.

12. Done.

13. Done.

14. We have added a legend to the figure.

15. Corrected.

16. The answer to this point is given in the response to point 11. We have added the following sentence to the manuscript to make it clearer: "Nonetheless, the heating cycles that each sample has gone will remove the thermal history that the sample experienced during its synthesis, resulting in sample equilibration at conditions similar to atmospheric under argon flow to prevent oxidation."

17. The values of Tgonset and Tgliquid are used in the manuscript were calculated in the most accurate way from the heat capacity data according to the configurational entropy theory.
Other papers show the effect of heating/cooling rates on the glass transition temperatures and the specific viscosity values associated with it (e.g. Giordano et al., 2005, 2008b). Taking Tg as the temperature where viscosity is 1012 Pa s is just a comfortable approximation used in industrial science to compare it at the timescale of forming processes (about 100-1000 s) and is used here for convenience as it can be calculated from viscosity measurements. Industry actually defines 1012.2 Pa s viscosity value as the “annealing point”. There are two standard ASTM measurements using fiber elongation and beam bending techniques (ASTM C336 and C1350M).

18. The Tgonset of a glass which was previously cooled at 10K/min through the glass transition temperature region and subsequently heated up at 10K/min will exhibit Tgonset equal to the temperature where viscosity is ~1012 Pa s. This seems to be universal in oxide and silica base glasses.

REVIEWER 2.

Line 148: A column reporting the values of the mass of the samples investigated in this work has been added to Table 1 and the text has been changed accordingly.

Line 154: We have slightly modified the text (lines from 169 to 178) to provide some additional information about the DSC experimental procedure.

Line 157: We have added a small paragraph (lines 179 to 186 in the revised manuscript) to explain how many thermal cycles the samples experienced and how the samples were inspected to check for any potential change/instability due to the thermal treatments.

Line 173: We have added some more details (lines 179- 186) described how we checked sample stability after the DSC experiments.

Line 182: We have added a legend to Fig. 2b.
With regard to error bars, we have added the following sentence on lines 156-158: " Based on multiple heating and cooling scans we believe reproducibility to be better than 3%. Therefore error bars for the Cp values of the fully relaxed liquid (Cpl) or Cp values of the glass (Cpg) are smaller than the symbol size used in the figures."
With regard to the number of measurements, yes, the presented data are based on one measurement at matching cooling and heating rates of 10 K/min for each sample. However, each sample experienced multiple thermal cycles (see lines 175-184 for a more detailed description of the measurement procedure) and inspected the samples before and after the DSC experiments.

Line 200: See previous comment and lines 146 - 158.

Lines 230 to 233 and line : We have modified the text and added a reference to Di Muro et al. (2009) who measured the redox state of various glasses (basalts in particular). Please also see comment to reviewer #1 (point 1).

Line 263: Letters were added to each figure in order to identify panels. Thank you for the suggestion.

Line 275: Legend was added for sake of clarity as suggested by the reviewer. Thank you.

Line 282-287 (now 312): The word "minima" was referred to trends observed in Fig. 4B. We have slightly modified the text in order to clarify it.

Lines 323-325 (now line 354-357 and added new text from line 358 - 378): here we have explained (having significantly extended the database of comparison for the heat capacity of hydrous melts compared to the previous work by Bouhifd et al. 2006, 2013) on which statistical parameters (standard deviation and average relative error) we decided to choose a best fit value of 79 J mol-1 K-1 for the partial molar heat capacity of water. We also explain that the difference between our value and the value of 85 J mol-1 K-1 proposed by Bouhifd et al. (2006) is rather insignificant. However, the value of 257 J mol-1 K-1, proposed by Bouhifd et al. 2013 does not reproduce the data as well using all models.

Lines 326 - 343: We have inserted a new paragraph describing the glass transition variation.

Line 464: we replaced steeply with steadily.

Heat capacity of *hydrous* trachybasalt from Mt Etna: comparison with $CaAl_2Si_2O_8$ (An) – $CaMgSi_2O_6$ (Di) as basaltic proxy compositions

D. Giordano[a], A.R.L. Nichols[b], M. Potuzak[c], D. Di Genova[d], C. Romano[e] and J.K. Russell[f]

[a] Dipartimento di Scienze della Terra, Universita' degli Studi di Torino, Via Valperga Caluso 35, 10125 Torino, Italia

[b] Research and Development Center for Ocean Drilling Science, Japan Agency for Marine Earth Science and Technology (JAMSTEC), 2-15 Natsushima-cho, Yokosuka, Kanagawa, 237-0061, Japan

[c] Science and Technology Division, Corning Incorporated, Corning, 14831 NY, USA

[d] Department for Earth and Environmental Sciences, University of Munich, Theresienstraße 41/III, 80333 Munich, Germany

[e] Dipartimento di Scienze, Università degli Studi Roma Tre, L.go San Leonardo Murialdo 1, 00146 Rome, Italia

[f]Department of Earth, Ocean and Atmospheric Sciences, The University of British Columbia, Vancouver, British Columbia, V6T 1Z4

Corresponding author details

phone: +39 011 670 5110

fax: +39 011 670 5128

e-mail: daniele.giordano@unito.it

Keywords: specific heat, Etna trachybasalt, anorthite-diopside, hydrous silicate melts

Submitted to

Contributions to Mineralogy and Petrology

January 20, 2015

Revised September 24, 2015

Abstract

The specific heat capacity (C_p) of six variably-hydrated (~ 3.5 wt% H_2O) iron-bearing Etna trachybasaltic glasses and liquids has been measured using differential scanning calorimetry from room temperature across the glass transition region. These data are compared to heat capacity measurements on thirteen melt compositions in the iron-free anorthite (An) - diopside (Di) system over a similar range of H_2O contents. These data extend considerably the published C_p measurements for hydrous melts and glasses. The results for the Etna trachybasalts show non-linear variations in, both, the heat capacity of the glass at the onset of the glass transition (i.e. C_p^g) and the fully relaxed liquid (i.e. C_p^l) with increasing H_2O content. Similarly, the "configurational heat capacity" (i.e. $C_p^c = C_p^l - C_p^g$) varies non-linearly with H_2O content. The An-Di hydrous compositions investigated show similar trends, with C_p values varying as a function of melt composition and H_2O content. The results show that values in hydrous C_p^g, C_p^l and C_p^c in the depolymerized glasses and liquids are substantially different from those observed for more polymerized hydrous albitic, leucogranitic, trachytic and phonolitic multicomponent compositions previously investigated by Bouhifd et al. (2006). Polymerized melts have lower C_p^l, C_p^c and higher C_p^g with respect to more depolymerized compositions. The covariation between C_p values and the degree of polymerization in glasses and melts is well described in terms of a modified $SM_{hydrous}$, and $NBO/T_{hydrous}$. Values of C_p^c increase sharply with increasing depolymerization up to $SM_{hydrous}$ ~30-35 mol % ($NBO/T_{hydrous}$ ~ 0.5) then decrease to an almost constant value.

The partial molar heat capacity of H_2O for both glasses ($C_p^g{}_{H2O}$) and liquids ($C_p^l{}_{H2O}$) appears to be independent of composition and, assuming ideal mixing, we obtain a value for $C_p^l{}_{H2O}$ of 79 J mol^{-1} K^{-1}. However, we note that a range of values for $C_p^l{}_{H2O}$ (i.e. ~ 78 - 87 J mol^{-1} K^{-1}) proposed by previous workers will reproduce the extended data to within experimental uncertainty. Our analysis suggests that more data are required in order to ascribe a compositional dependence (i.e. non-ideal mixing) to $C_p^l{}_{H2O}$.

1. Introduction

The thermophysical properties of silicate melts are of fundamental importance for the characterization of the dynamics and energetics of silicate melts on Earth. Heat capacity is one such property and the isobaric heat capacities of silicate glasses and liquids are important for thermal modelling of magmatic and volcanic processes (i.e., mingling and mixing, partial melting and solidification, advection of heat, degassing) (e.g. Burnham and Davis, 1974; Clemens and Navrotsky 1987; Russell 1990; Sahagian and Proussevich 1996; Perugini and Poli 2005), to the energy budgets of volcanic eruptions (e.g. Pyle 1995), and for constraining phase equilibria models (Sack and Ghiorso 1989; Ghiorso and Sack 1995). Perhaps more importantly, they provide an important linkage between macroscopic thermochemical properties of melts and their corresponding structural and transport properties (e.g. Richet and Bottinga 1995; Giordano et al. 2009; Chevrel et al. 2013).

Several studies have investigated the specific heat capacity (C_p) of anhydrous (i.e. H_2O <500 ppm) melts (e.g., Navrotsky, 1995; Toplis et al. 2001). However, given the inherent difficulties in conducting equivalent experiments on hydrous melts, only a few studies (i.e. Giordano et al. 2005, 2008a; Bouhifd et al. 2006; 2013, Di Genova et al. 2014) have measured the calorimetric properties of hydrous multicomponent melts to date. Previous calorimetric measurements (Clemens and Navrotsky; 1987) and thermodynamic modeling (Burnham and Davis, 1974) of the albite-H_2O system estimated the partial molar heat capacity of dissolved H_2O in silicate liquids ($C_p{}^l{}_{H2O}$) at between 78 and 87 J mol^{-1} K^{-1}.

All previous studies investigated *iron-free* multicomponent hydrous silicates and established that the contribution of H_2O to the C_p of silicate glasses is small, temperature dependent, and largely independent of composition. Bouhifd et al. (2006) investigated hydrous, silica-rich, polymerized melt compositions, including phonolite, trachyte, leucogranite and albite, and reported $C_p{}^l{}_{H2O}$ as independent of melt composition and to have a value for 85 J mol^{-1} K^{-1}. In contrast, a more recent paper by Bouhifd et al. (2013) investigating silica-poor, hydrous, depolymerized compositions (i.e., tephritic and foiditic) reported a value for $C_p{}^l{}_{H2O}$ of H_2O of 237+/-40 J mol^{-1} K^{-1}. The authors ascribed this difference in estimated values to a strong compositional dependence of the partial molar heat capacity of H_2O. The contradiction between the Bouhifd studies and the previous studies (Burnham and Davis, 1974; Clemens and Navrotsky, 1987) highlights the need for further investigations to establish what role H_2O plays in determining the C_p of multicomponent hydrous liquids and glasses and how this can be parameterized and modeled.

Here we have investigated the heat capacities of hydrous glasses and liquids of a natural trachybasalt from Etna and of liquids along the An-Di join. The viscosities and glass transition temperatures for these melts were previously measured by Giordano and Dingwell (2003) and Giordano et al. (2005, 2008), respectively. The compositions investigated here were chosen for three main reasons. The composition of the Etna trachybasalt represents one of the most common natural volcanic rock compositions on Earth. It is iron-bearing and H_2O-bearing and has glass-forming ability easily detectable by differential scanning calorimetry (DSC) (e.g. Giordano et al. 2005; Potuzak et al. 2009). Secondly, the An-Di-H_2O system is of general interest to geochemists as well as to petrologists because it serves as a simple analogue for basaltic compositions (e.g., Bowen, 1915; Kushiro, 1973; Weill et al. 1980; Navrotsky et al. 1980). In this study we test the degree to which An-Di liquids are good analogues for basalts by comparing the measured calorimetric properties of hydrous trachybasaltic glasses and liquids with those in the An-Di-H_2O system. Thirdly, the wide range of compositions investigated here allows us to explore other thermochemical properties of hydrous silicate melts. We finally combined these measurements with the corresponding viscosity datasets in order to model the configurational entropies at the glass transition and establish the correlation between transport and thermochemical properties according to the Adam and Gibbs theory of configurational entropy.

2. Experimental methods

2.1. Sample description

The methods used to synthesize the samples and characterize their compositions and H_2O contents are well established in the literature (e.g., Giordano and Dingwell, 2003; Giordano et al. 2005; 2008) and, thus, only briefly summarized here. The starting materials for the hydrous melts in the An-Di system belong to a selection of dry glasses used by Knoche et al. (1993) and have the following compositions: $An_{10}Di_{90}$, $An_{42}Di_{58}$, $An_{90}Di_{10}$ and An_{100} (Giordano et al. 2008). The starting material for the Etna trachybasalt is from Giordano and Dingwell (2003). H_2O-bearing samples, containing up to ~ 3.5 wt% H_2O were synthesized using an internally heated pressure vessel at the IMH (Institute of Mineralogy, University of Hannover, Germany) and the piston cylinder apparatus available at the BGI (Bavarian Geoinstitute, University of Bayreuth, Germany). The run products consisted of crystal-free, translucent glasses with no visible bubbles.

After high pressure syntheses, the samples were cut into 0.3 to 1 mm thick disks and doubly polished in preparation for calorimetry measurements. Compositions are reported in previous works from Giordano et al. (2005, 2008) and calculated compositional parameters for the investigated samples are reported in Table 1. Prior to the calorimetry measurements, the distribution, homogeneity and absolute H_2O content of the disks were measured using FTIR spectroscopy and Karl-Fisher Titration (KFT), the latter following the method described by Behrens et al. (1996). The measured H_2O contents are reported in Table 1 together with their associated uncertainties (corrected for 0.17 wt% unextracted H_2O; cf. Behrens et al. 1996).

2.2. Calorimetric heat capacity measurements of glasses and liquids

Calorimetry measurements were performed using a differential scanning calorimeter (NETZSCH® DSC 404 Pegasus) at the Department of Earth and Environmental Sciences, University of Munich, Germany, under high purity argon gas to prevent oxidation of iron. The thermocouples of the DSC were calibrated using the transformation temperatures of the standard salts, $RbNO_3$, $KClO_4$, CsCl and K_2CrO_4. The sensitivity of the DSC was calibrated using a single sapphire crystal standard. A baseline heat flow was established by measuring the calorimetric response of two empty Pt/Rh crucibles in order to be able to calculate C_p. Then the heat flow of a single sapphire crystal, placed in one of the crucibles, against the empty crucible was measured. The DSC was calibrated at standard heating rate of 10K/min with the sapphire disk cut from single crystal sapphire perpendicular to the crystalline c-axis. Both upper and lower flat surfaces were polished in order to achieve an excellent contact and heat transfer between the platinum crucible and the sapphire disk placed flat on the bottom of the crucible. A comparison between the multiple calibration runs performed by using our calorimeter are reported in Fig A (supporting material online) compared with the ASTM E1269-5 reference standard. This figure shows that there was an excellent agreement between the reference C_p data and our own measurements performed up to 1261 K (Fig A, supporting online material). The accuracy of the experiments was calculated to be within +/- 1% (Fig. B, supporting online material).. Based on multiple heating and cooling scans we believe reproducibility to be better than 3%. Therefore error bars for the C_p values of the fully relaxed liquid (C_p^l) or C_p values of the glass (C_p^g) are smaller than the symbol size used in the figures.

Finally, the heat flow of a doubly polished glass sample disk (or portion of a disk), placed in one of the crucibles, was measured against the empty crucible. The masses of the sapphire standards used in the experiments were 27.77 or 55.90 mg; the mass of the sample analysed was as close to this as possible. Commonly the masses of the samples were matching the mass of sapphire standard, used as a calibration material for C_p , within the $\pm$15% . In the case of sample 802 only, due to the scarcity of available material, the mass was half that of the standard. We decided to keep the data related to this sample because it agrees with the overall pattern exhibited by the other Etna samples measured here and in Di Genova et al (2014). Heating across the glass transition into the supercooled liquid region started at 40 °C and was conducted cooling/heating at 1 atm under high purity argon gas to prevent oxidation of iron (Giordano et al. 2005, 2008). In order to allow complete structural relaxation, samples were initially heated above the glass transition temperature into the supercooled liquid field (Fig. 1) where the sample relaxed removing any memory of its thermal and high pressure history obtained during experimental synthesis (Giordano et al. 2008a). This initial heating was conducted at 20 K/min (for the Etna samples) and 10 K/min (for the An-Di samples). Then the sample was cooled to 40 °C at 20 K/min before being heated above the glass transition temperature again at a matching heating rate. This cooling and heating cycle was repeated three more times at matching cooling and subsequent heating rates of 15, 10, 5 K/min. The time spent above the glass transition temperature during each thermal cycle was kept at a minimum (on the order of 100 s) in order to prevent H_2O exsolution. After the measurements were completed for each sample, the sample was removed from the DSC at room temperature and thoroughly inspected via optical microscopy for a) clarity b) formation of defects, such as bubbles, crystalline phases and microscopic phase separations. Additionally the dissolved water content of the sample that had undergone the DSC experiments was measured by FTIR and compared with the original sample. Here we only report data from those samples that did not exhibit any changes after having undergone the four thermal cycles during the DSC measurements. The C_p values for the glass and liquid were determined based on the measurements conducted during heating at 10 K/min after cooling at the same rate.

Figure 1 shows the variation of C_p as a function of temperature for one of the investigated samples cooling/heating during heating at 10 K/min after cooling at 10 K/min. The C_p of the glass (C_p^g) at the temperature of the onset of the glass transition (T_g^{onset}) is calculated by fitting a Maier–Kelley (MK) equation (C_p^g = a+bT+c/T^2+d*T^0.5; where T is the absolute temperature and a, b, c, d are adjustable parameters, Maier–Kelley, 1932) to the part of the C_p-curves preceding the onset of the glass transition ($<T_g^{onset}$). The parameters used in the MK equation for each of the investigated samples are provided in Table 1. The MK curve is extrapolated to T_g^{onset}, which is defined as the temperature at which the extrapolated C_p^g intersects the extrapolated rapid increase in C_p associated with the glass transition, as described by Moynihan (1995). C_p^l is defined as the C_p of the fully relaxed liquid at the temperature of the stable liquid (T_g^{liquid}) in the heat capacity curve, and the "configurational heat capacity", C_p^c, is defined as the difference between C_p^l and the C_p^g.

Values of T_g^{onset} and T_g^{liquid} for the Etna trachybasalts and for the An-Di samples are reported in Table 1. Values at T_g^{onset} (Giordano et al. 2005; Giordano et al. 2008) and T_g^{liquid} (this study) were used to calculate C_p^g and C_p^l according to the model of Richet (1987) and Richet and Bottinga (1985), which assumes that the partial molar heat capacities of Al_2O_3 and TiO_2 depend on temperature.

3. Results

3.1. Effects of H_2O on the C_p of Etna and An-Di glasses and liquids

The measured C_p^g, C_p^l and C_p^c values are reported in Table 1 and their variations as a function of composition are discussed below.

3.1.1. Specific heat capacity of hydrous glasses (C_p^g)

For all compositions investigated, increased H_2O content causes a small decrease in C_p^g (Fig. 2) defining a slight curving upwards trend. Fig. 2a shows that the C_p^g of the Etna trachybasalts (dashed curve and empty triangles) has only a minor decrease (~7 %), from about 75.8 to 70.5 $Jmol^{-1}.K^{-1}$ for H_2O content up to 2.31 wt% (6.92 mol%). Further addition of H_2O up to 3.46 wt% (11.39 mol%) produces a slight increase in C_p^g to 71.5 J mol^{-1} K^{-1}. Sample An_{10} also exhibits a slight increase in C_p^g, from 59.9 to 61.4 J mol^{-1} K^{-1}, upon addition of H_2O from 1.75 to 2.58 wt% (5.26 to 7.62 mol%) (Fig. 2b). All other samples along the Di-An join show a small but systematic decrease in C_p^g with H_2O. In general (Fig. 2b), the glasses of the An-Di system show parallel patterns that mimic that followed by Etna trachybasalt (dashed curves). The absolute values of C_p^g are very similar for An_{100}, An_{90} and Etna (dashed curve) whereas they decrease slightly but systematically for An_{42} and An_{10} compositions. For instance, at 5 mol% H_2O, C_p^g of An_{100}, An_{90}, Etna, An_{42}, An_{10} are calculated to be ~ 77, 74, 72, 66 and 60 J mol^{-1} K^{-1}, respectively (see Table 1 for C_p values). The dissolution of H_2O produces proportionally significantly different results in the C_p^g for the samples investigated (Table 1). The maximum decrease of C_p^g observed for Etna trachybasalt, An_{10} and An_{42}

are 5, 10, and 10 J mol^{-1} K^{-1}, corresponding to 7%, 12%, and 14% reductions in the initial anhydrous values, are due to the addition 11.4, 10.3 and 8.5 mol% H_2O, respectively.

3.1.2. Specific heat capacity of hydrous liquids (C_p^l) and the configurational heat capacity (C_p^c)

The variation of C_p^l with H_2O content in the Etna trachybasalt shows a smooth curving downward pattern. Opposite to the pattern observed for C_p^g, C_p^l decreases only slightly (from 97.9 to 96.3) up to 2.31 wt% (7.82 mol%) H_2O, then shows a steeper decrease (from 96.3 to 92.4) from 2.31 to 3.46 (11.39 mol%) wt% H_2O. Small effects (up to a maximum of ~ 8% for An100) are also observed for samples in the An-Di system. The effect of dissolved H_2O on the C_p^l values for the An-Di system shows similar relationships to those observed for C_p^g, with An_{100} and An_{90} having similar to slightly higher C_p^l values with respect to the Etna trachybasalt C_p^l values at the same H_2O content, while the values for An_{42} and An_{10} at the same H_2O content are systematically lower (Table 1). For all investigated samples, the initial dissolution of H_2O in the anhydrous melt compositions produces an increase in the C_p^c values. Moreover C_p^c for the Etna trachybasalt shows a concave trend as a function of H_2O (Fig. 2). This trend is determined by a progressive increase of C_p^c from 21.6 up to 25.8 J mol^{-1} K^{-1}, due to the addition of 2.31 wt% H_2O, followed by a sharp decrease to 20.9 J mol^{-1} K^{-1}as H_2O content further increases up to 3.46 wt%. This decrease is visible only for the Etna trachybasalt, maybe due to the greater amount of H_2O dissolved in this liquid compared to the other samples analyzed. An_{100} contains almost the same amount of H_2O as the Etna samples. In detail, the maximum variation in C_p^c due to the addition of H_2O is different for each dataset, from ~ +40% for the An_{10} sample; +/-20% for Etna and ~ +13% for An_{42}. Given the limited number of data available, the C_p^c variations for An_{100} and An_{90} are more difficult to evaluate as these datasets consist of only two points (Table 1).

3.2. C_p variations of hydrous melts and glasses with composition (*$SM_{hydrous}$*, *$NBO/T_{hydrous}$*)

In order to evaluate the effect of structure on the C_p of the investigated systems, we calculated, for both dry and hydrous compositions, the structure modifier (*SM*; Giordano et al. 2009) and the non-bridging oxygen over tetrahedra (*NBO/T)* parameters, assuming H_2O as a network modifier. The modified *SM* parameter, referred to hereafter as $SM_{hydrous}$, is calculated, in mol%, as the sum of the network modifier oxides plus the amount of dissolved H_2O (Giordano et al. 2009; Mercier et al. 2009), without accounting for H_2O speciation. The modified *NBO/T* parameter, $NBO/T_{hydrous}$, is calculated assuming all hydrogen is in a network modifier role. Both the $SM_{hydrous}$ and $NBO/T_{hydrous}$ are considered to be representative of the degree of polymerization of the hydrous liquids (Mysen, 1988; Giordano et al. 2009). In our calculation, iron was partitioned following the principles of Mercier et al. (2009), who assumed an average iron oxidation state ratio of 0.5 for dry samples quenched in air. For the hydrous samples synthesized in pressure vessels the iron oxidation state was not directly determined, and we arbitrarily chose the same average iron oxidation state ratio of 0.5. The latter value is realistic and fits with the average iron oxidation state of most of the synthesised anhydrous glasses (Di Muro et al., 2009).

Figure 3 illustrates how C_p^g, C_p^l, and C_p^c vary as a function of these parameters, in a compositional regime encompassing more polymerized to more depolymerized glasses/liquids. By observing the heat capacity variation in the different compositional domains of Fig. 3 ($SM_{hydrous}$, $NBO/T_{hydrous}$), the trends of Fig. 2 are more evident. In particular, C_p^l and C_p^g decrease smoothly as a function of $SM_{hydrous}$ and $NBO/T_{hydrous}$, with values decreasing from An_{100} ($SM_{hydrous}$ =26.1; $NBO/T_{hydrous}$ = 0.04) to An_{90} ($SM_{hydrous}$ =31.5; $NBO/T_{hydrous}$ = 0.25); Etna trachybasalt ($SM_{hydrous}$ = 33; $NBO/T_{hydrous}$ = 0.47); An_{42} ($SM_{hydrous}$ =39.5; $NBO/T_{hydrous}$ = 0.83) and An_{10} ($SM_{hydrous}$ =45.3; $NBO/T_{hydrous}$ = 1.50). Sample An_{10} is somewhat anomalous as it shows a slight increase (~ 2.5% of the measured value) of C_p^l and C_p^g, as already shown in Fig. 2b. C_p^c, on the other hand, shows a slight increase with increasing the degree of depolymerization. These trends suggest that, for the samples investigated here, C_p^g, C_p^l and C_p^c can be, to a first approximation, described in terms as a function of $SM_{hydrous}$, $NBO/T_{hydrous}$.

Variations in C_p^l and C_p^g as a function of these compositional parameters define relative minima at $SM_{hydrous}$ ~45 mol%, $NBO/T_{hydrous}$ ~1.2; a minimum is not observed in the variation of C_p^c. In order to interpret and rationalize this behaviour, we have expanded our analysis (Fig. 4) to include other published data for more polymerized and depolymerized hydrous melt compositions (Bouhifd et al. 2006; Bouhifd et al. 2013). Data from Di Genova et al (2014) for the Etna trachybasalt agree well with our measurements (see Table 2) and are plotted in Fig. 4 with the same symbols (but smaller size) as our data for Etna.

4. Discussion

4.1. Heat capacity of glasses and liquids

4.1.1. Comparison with previous data

Our data on hydrous iron-bearing natural trachybasalt and synthetic An-Di compositions are compared with measurements on iron-free and iron-bearing compositions that are both more polymerized (i.e., albite, phonolite, trachyte, pantellerite) (Bouhifd et al. 2006, Di Genova et al. 2014) and less polymerized (i.e., tephrite, basalt, latite, foidite) (Bouhifd et al. 2013, Di Genova et al. 2014).

Figure 4 shows how C_p^g, C_p^l and C_p^c vary as a function of H_2O (panel A) and the $SM_{hydrous}$ parameter (panel B). Largely, it appears that polymerized melts have higher C_p^g values and lower C_p^l and C_p^c than the Etna trachybasalts and the other more depolymerized multicomponent melts. An increase in the $SM_{hydrous}$ parameter causes the C_p^c of polymerized and depolymerized melts to increase, although its effect on depolymerized melts is significantly smaller. In general, it appears that C_p^c increases up to $SM_{hydrous}$ of about 30 – 35 mol%, whereas any further increase in $SM_{hydrous}$ affects C_p^c to a smaller extent. The depolymerized tephritic and foiditic samples measured by Bouhifd et al. (2013) have, apart from the samples with the highest H_2O contents (Teph 2.2, NIQ 1.8), C_p^c values similar to those measured for the Etna trachybasalt and An-Di compositions (Table

1). On the contrary, C_p^g, C_p^l of tephritic compositions (Teph, NIQ), and similarly sample An_{10}, show a marked departure from the trends observed for the Etna trachybasalt. On the other hand, the pattern followed by C_p^c for these samples, although a bit steeper, appears to follow the overall path followed by the other compositions. Fig. 4A shows more clearly the effect of H_2O has on the C_p data of more depolymerized compositions (Teph, NIQ) measured by Bouhifd et al (2013) compared to the Etna trachybasalt. It shows that, apart from the C_p^l of sample Teph 2.2, the overall effect of H_2O on C_p of these depolymerized compositions is similar to, and substantially follows the same paths, as those of the Etna trachybasalt, although the C_p of these samples has only been measured at low H_2O contents. It is important to note that the trend of C_p^l for the FR latite sample (Di Genova et al. 2014) apparently shows a deviation from the overall trend.

The relative minima observed in Fig 4b for C_p^l and C_p^g generated by fitting the hydrous An-Di compositions persist even after adding the data from Bouhifd et al. (2013) and Di Genova et al. (2014). The reason for the minima are unclear; they could really represent a local minimum with underlying structural reasons, but they could also be a result of peculiar behaviour of the simplified hydrous An-Di compositions, fitting limitations, or an artifact of expressing composition in terms of $SM_{hydrous}$, $NBO/T_{hydrous}$ and the molar mass parameters.

4.1.2. Partial molar heat capacity of H_2O of silicate glasses ($C_p^g{}_{H2O}$) and liquids ($C_p^l{}_{H2O}$)

We have compared our results with previous models for anhydrous glasses (Richet, 1987) and for anhydrous liquids (Richet and Bottinga, 1985; Lange and Navrotsky, 1992; Stebbins et al. 1984). We have modified these models to account for the effects of H_2O (using the partial molar heat capacity of H_2O in silicate glasses, $C_p^g{}_{H2O}$, and liquids, $C_p^l{}_{H2O}$) using the approach of Bouhifd et al. (2006; 2013) and Di Genova et al. (2014).

In general, the Richet (1987) model shows that the heat capacity of the glasses can be predicted by the following additive function of composition:

$$C_p^g = \sum x_i \, C_p^g{}_i(T) \qquad (1)$$

where x_i is the mole fraction of oxide and $C_p{}^g{}_i$ is the partial molar heat capacity of oxide *i* in the glass which depends on temperature (Richet, 1987).

Measured and calculated $C_p{}^g$ for anhydrous and hydrous glasses are within error of the values expected using the model. Given the fact that the Richet (1987) glass model is calibrated on a database significantly larger than that of our study, we assume that it provides the most accurate estimates of $C_p{}^g{}_i$ for anhydrous glasses available so far. For hydrous glasses we assume that the temperature dependence of $C_p{}^g{}_{H2O}$ is well represented by the equation obtained by Bouhifd et al. (2006), which assumes it is independent of composition.

The $C_p{}^l$ measured here and in the previous work by Bouhifd et al. (2006; 2013) for hydrous compositions have been compared with predictions made using the models for anhydrous compositions from Stebbins et al. (1984), Richet and Bottinga (1985), implemented for the temperature dependent partial molar heat capacity of Al_2O_3 as obtained by Courtial and Richet (1993), and Lange and Navrotsky (1992). In the subsequent discussion these models will be referred to as S`84, RBC`85,93 and LN`92, respectively. We have also compared the measured $C_p{}^l$ with those predicted using $C_p{}^l{}_{H2O}$ obtained by Bouhifd et al. (2006; 2013) combined with the above mentioned S`84, RBC`85,93 and LN`92 models. In our calculation, iron was partitioned following the principles of Mercier et al. (2009), who assumed an average iron oxidation state ratio of 0.5 for dry samples quenched in air. For the hydrous samples synthesized in pressure vessels the iron oxidation state was not directly determined, and we arbitrarily chose the same average iron oxidation state ratio of 0.5. Nonetheless, the heating cycles that each sample has gone will remove the thermal history that the sample experienced during its synthesis, resulting in sample equilibration at pressure conditions similar to atmospheric under argon flow to prevent oxidation.

Table 1 shows the predicted $C_p{}^l$ values using the S`84, RBC`85,93 and LN`92 models. The calculations were performed using the $C_p{}^l{}_{H2O}$ of 85 J mol^{-1} K^{-1}, proposed by Bouhifd et al. (2006), the $C_p{}^l{}_{H2O}$ of 237 J mol^{-1} K^{-1}estimated by Bouhifd et al. (2013) and the $C_p{}^l{}_{H2O}$ of 41 J mol^{-1} K^{-1} estimated by Di Genova et al. (2014).

Our parameterization based on the data compiled here (Table 1) and based on the minimization of standard deviation and relative errors suggests an optimal value for $C_p{}^l{}_{H2O}$ of 79 J mol^{-1} K^{-1}. This value is in close agreement with the early studies of Burnham and Davis (1974) and Clemens and Navrotsky (1987) and provides a better fit to the data than other values (e.g., Table 1).

In particular, the $C_p{}^l{}_{H2O}$ of 79 J $mol^{-1}K^{-1}$ reduces the deviation from model calculations to 1.6%. $T_g{}^{liquid}$ used to calculate $C_p{}^l$ by the RBC`85,93 model are reported in Table 1.

If instead all the data measured in this study and the Bouhifd et al. (2006, 2013) studies are considered, the RBC`85,93 and S`84 models using either the $C_p{}^l{}_{H2O}$ defined here (79 J/mol*K) or by Bouhifd et al. (2006) (85 J/mol*K), reproduce the data equally well. Results using both the RBC`85,93 and S`84 models are based on the minimization of the average relative error (3.7%). In particular, the $C_p{}^l$ measured in this work are best reproduced by the RBC`85,93 model (to within 1.1% and 1.9 % relative error for the Etna trachybasalt and the Anorthite-Diopside join). The largest difference between the measured and predicted values is observed for the Teph 2.2 liquid measured by Bouhifd et al. (2013) (Table 1).

If we consider single datasets, the data obtained in this study are better described by the RBC`85,93 model. On the other hand, this is not true if we include in our analysis the data from Bouhifd et al (2006, 2013). In this case, the phonolitic and trachytic compositions investigated by Bouhifd et al (2006) are better reproduced by the LN '92 model, whereas the albitic liquid is best reproduced by the S '84 model. Finally, the tephritic and foiditic compositions are better reproduced by the S'84 model. In every case it did not matter whether the $C_p{}^l{}_{H2O}$ defined in this study or that defined by Bouhifd et al. (2006) was used.

4.1.3. Relationships between $T_g{}^{onset}$, $T_g{}^{liquid}$ and $T_g{}^{12}$

Figure 5A compares $T_g{}^{onset}$ with $T_g{}^{liquid}$ and includes data presented here and from Giordano et al. (2005; 2008) and Bouhifd et al. (2006; 2013). $T_g{}^{onset}$ with $T_g{}^{liquid}$ show a strong positive correlation with a slope of 1 and an intercept value of ~58 K, which represents the average ΔT over which the glass to melt transition is measured. To a first approximation the correlation between

T_g^{onset} and T_g^{liquid} is clearly independent of composition and H_2O content (Giordano et al. 2005, 2008). We have also plotted the calorimetrically measured values of T_g^{onset} against model values of T_g^{12}, the glass transition temperature, as calculated from Adam Gibbs model values at viscosity of 10^{12} Pa s (see § 4.2; Table 2) in Fig. 5B. There is clear agreement (see Appendix) between the calorimetric (observed) and predicted (modeled) glass transition temperatures.

4.2. Configurational contribution

4.2.1. Relationship with the viscosity of silicate melts

The capacity of liquids to adopt different structural configurations as a function of temperature distinguishes them from solids. Indeed, the difference in heat capacity between a glass and the corresponding fully relaxed liquid at the limiting fictive temperature is a direct record of these configurational changes. Classically, it is referred to as the configurational heat capacity C_p^c and there is a corresponding configurational entropy (S^c) (the same as macroscopic entropy) that is functionally dependent on C_p^c (e.g. Richet, 1987; Richet and Bottinga, 1985, 1995 and Toplis et al. 2001). These thermochemical properties (i.e. S^c and C_p^c) reflect the changes in structural state of the melt as it transitions to a glass, and the Adam and Gibbs theory (Adam and Gibbs, 1965) provides a connection to the temperature dependence of melt viscosity by:

$$\log \eta = A_{AG} + B_{AG} / (T\, S^c(T)) \qquad (2)$$

The variables include the pre-exponential term A_{AG}, the potential energy barrier hindering the structural rearrangement of the liquid B_{AG}, and the configurational entropy of the liquid at a temperature of interest ($S^c(T)$). The variable $S^c(T)$ represents a measure of the number of configurations accessible to the liquid and can be related to the configurational energies at the glass transition temperature (T_g) by the expansion:

$$S^c(T) = S^c(T_g) + \int_{Tg}^{T} (C_p^c / T)\, dT \qquad (3)$$

We have used the complementary viscosity data available for the melts listed in Table 2 to obtain model estimates of $S^c(T_g)$. We mainly follow the work of Richet (1984), Toplis et al. (1997), Toplis (1998) and Webb (2008), wherein Eq. 1 is fitted to measurements of C_p^c and melt viscosity for the same melt compositions (Giordano et al. 2005, 2008; Whittington et al. 2000, 2001) and the adjustable parameters are A_{AG}, B_{AG} and $S^c(T_g)$. A full description of our optimization philosophy and methodology is provided in the Appendix where we remodel a subset of the data analyzed by Toplis et al. (1997). The main and most important difference in our approach is that we assume that A_{AG}, the pre-exponential term in Eq. 1, is a constant for all melts. The variable *A*, in most conventional equations describing the temperature dependence of melt viscosity, represents the high temperature limits to viscosity. This value has been shown theoretically and empirically to be a constant value for all silicate melts and, thus, independent of composition by Russell et al. (2002; 2003), Russell and Giordano (2005), Giordano and Russell (2007) and Giordano et al. (2008b).

Operationally we combined all datasets (k=23) comprising measured values of C_p^c, onset values of T_g, and melt viscosity measurements at four or more temperatures to create a single overdetermined system of non-linear equations (n=292). The adjustable parameters included: a single common unknown value of A_{AG} and k values of B_{AG} and $S^c(T_g)$, each (2*k+1 = 47). We then applied the optimal value of A_{AG} (-3.51) to model the other melt compositions that had fewer than four temperature measurements of viscosity (k' = 18; Table 2). Specifically, we fitted Eq. 1 to the data available for individual melt compositions assuming that A_{AG} = -3.51 to retrieve optimal values of B_{AG} and $S^c(T_g)$ for these melts. This two-pronged modeling strategy put all model parameters on the same platform (e.g., a common value of *A* for the high temperature viscosity limit) and thereby, avoided problems that arise from using an arbitrary value of A_{AG}, (cf. Toplis et al. 1997; Webb 2008).

The results of our optimization for best fit values of A_{AG}, B_{AG} and $S^c(T_g)$ are illustrated in Figure 6A. Our model reproduces the original viscosity data to within measurement error (Fig. 6B). The range of model values of B_{AG} and $S^c(T_g)$ for a fixed value of A_{AG} of -3.51 is shown in Fig. 6A; $S^c(T_g)$ varies from 9 - 35 J mol^{-1} K^{-1} whilst B_{AG} ranges from 150 - 450 kJ mol^{-1}. The two parameters show a very strong positive correlation and part of this is a model-induced covariation (cf.

Appendix A; Russell et al. 2002). However, the range of values in Fig. 6A span a range much larger than the confidence ellipses arising from analytical uncertainties and the functional form of the equation, indicating that A_{AG} and B_{AG} are, in fact, positively correlated properties of these melts.

We have also discriminated the anhydrous (black symbols) from the hydrous (grey) melts and used the size of symbol to indicate the relative H_2O contents. Values of B_{AG} and $S^c(T_g)$ for the anhydrous melts are uniformly lower than for the H_2O-bearing melts. However, there is no single systematic pattern in B_{AG} and $S^c(T_g)$ values with increasing amounts of H_2O suggesting that the parameters are controlled by both melt composition and H_2O content, although the highest H_2O contents do suggest a decrease in values of B_{AG}.

On the basis of our model optimization we have calculated the derivative transport properties T_g^{12} and melt fragility (m). As developed by Toplis et al. (1997), these properties can be computed for each melt from the measured values of C_p^c and the model values of A_{AG}, B_{AG} and $S^c(T_g)$:

$$Tg^{12} = \frac{B_{AG}}{(12 - A_{AG})\, S^c(Tg)} \qquad (4)$$

and

$$m = [12 - A_{AG}] \left(1 + \frac{Cp^c}{S^c(Tg)} \right) \qquad (5)$$

respectively. The calculated values of T_g^{12} and fragility for the suite of 31 anhydrous (black symbols) and hydrous (grey symbols) melts are plotted in Figure 6C. The dataset describes a general trend that echoes the pattern predicted by the Giordano et al. (2008) viscosity model (cf. Fig. 6b in Giordano et al. 2008). The anhydrous melts show a range of fragilities 25-60 and a narrow range of model values of T_g^{12} (900-1150 K). The addition of H_2O causes a pronounced decrease in T_g^{12} values (600-900K) and has variable effects on melt fragility; although the reduced range of fragilities (20-45) for hydrous melts suggests that dissolved H_2O causes many melts to become more Arrhenian-like and stronger (Giordano et al. 2008b; 2009). These results are partially corroborated by Di Genova et al. (2014) who noticed that the effect of H_2O on fragility depends on the degree of polymerization of the anhydrous equivalent melt.

The addition of dissolved H_2O, on the order of 3 wt%, causes a marked increase (up to three-fold) in B_{AG} and $S^c(T_g)$ values for the An-Di and Etna melts, as well as, the more depolymerized compositions of Bouhifd et al (2013). A similar, but significantly less marked increase is observed for the more polymerized melts of Bouhifd et al. (2006). In this case B_{AG} increases only slightly whilst $S^c(T_g)$ increases to nearly double the anhydrous value.

Figure 7 shows how the ratio $B_{AG}/S^c(T_g)$ varies as a function of H_2O and $SM_{hydrous}$ and provides a means to explain, according to Eq. 1, the low viscosity of hydrous Etna trachybasalt relative to the An-Di-H_2O system**.** As H_2O content increases, in fact, the Etna trachybasalt shows the lowest $B_{AG}/S^c(T_g)$ values and consequently the lowest viscosity at the same H_2O (Fig 7A).

Fig. 7B shows how the $B_{AG}/S^c(T_g)$ ratio varies as a function of the $SM_{hydrous}$ parameter which largely represents the degree of polymerization. In the glass transition interval (where $S^c(T) \simeq S^c(T_g)$), the variation of the $B_{AG}/S^c(T_g)$ ratio largely follows (Eq. 1) the path of viscosity variation, meaning that, in that interval, lower $B_{AG}/S^c(T_g)$ values correspond to lower viscosities. Accordingly Fig. 7 shows the reason that the Etna trachybasalt has a viscosity lower than An-Di melts in the glass transition interval. The figure also suggests that higher $SM_{hydrous}$ values do not guarantee lower viscosity. An-Di melts, commonly considered highly depolymerized melts, have neither the lowest $B_{AG}/S^c(T_g)$ ratios nor the lowest viscosities.

The key to understanding the differences in behaviour between the multicomponent Etna compositions and the melts in the An-Di system resides in understanding the role of iron in the structure and thermodynamic quantities of natural silicate melts (Chevrel et al. 2013).

4.3. Structural considerations

For both dry and hydrous compositions, the variation in C_p^g observed among the different liquids are related to vibrational contributions, directly linked to the cation field strength, of chemical bonds in the structure (Giordano et al. 2008a, 2009). Therefore intuitively more depolymerised glasses will have longer and weaker Tetrahedra-Oxygen (TO) bonds associated with lower values of C_p^g. The trends visible in Fig. 3 and 4 are in perfect agreement with this consideration.

Trends in C_p^c can be discussed in more detail. In general, C_p^c is defined as the energy needed to change the structure of a liquid in response to temperature variations across the glass transition and it is made of a chemical and a topological contribution. The chemical contribution has to do with mixing of various chemical component in the silicate framework, (Al/Si order disorder, mixing of cationic sites, Q species equilibria triclusters, ion channeling, bond dangling, coordination state of network formers, coordination changes of network modifiers, etc. see Stebbins, 2008; Giordano et al. 2008a), whereas the topological contribution is related to the framework of the silicate network, therefore the configuration of the oxygen matrix, expressed in terms of TO bonds and TOT angle distribution.

It has previously been observed (Richet and Bottinga, 1985; Bouhifd et al. 1998; Toplis et al. 2001; Webb, 2008; Di Genova et al., 2014) that C_p^c increases with decreasing SiO_2. In general, this increase is ascribed to a decrease in the overall strength of TO bonds and to a correlated increase of the TO and TOT distribution (topological contribution to the configurational heat capacity). Second order variation in the C_p^c, at similar $NBO/T_{hydrous}$ or $SM_{hydrous}$ values, can be due to different Al/Si and/or alkali versus alkaline earth ratios.

The results shown in Fig. 4 are consistent with the increase in C_p^c as a function of the degree of depolymerisation of the melt that accompanies the decrease in SiO_2. The leveling off of C_p^c at $SM_{hydrous}$ ~ 30-35 mol% ($NBO/T_{hydrous}$~0.5) is more intriguing as it suggests that after a certain degree of depolymerisation, pertaining approximately to basaltic compositions, further increase in depolymerisation does not translate into a perceivable increase in the configurational heat capacity (or decrease in viscosity), as the increase in disorder (chemical or topological) does not have any appreciable effect on the energetics of an already extremely disordered/depolymerized liquid

(Giordano et al. 2008a). One possibility is that the observed leveling could be driven by stabilizing Al in lower coordination state (i.e., in Al[4] by alkalis or alkaline earth elements until the peraluminous melts become metaluminous (i.e., charge balanced)) and then further in peralkaline or peralkaline-earth field where Al starts to have higher coordination (C_N) and forming NBO on Si (Si-O-Al).

The introduction of H_2O in the silicate liquids seems to largely mimic the behavior of the other oxides (Fig 3 and 4). C_p^c seems to steadily increase as a function of H_2O content for polymerized compositions ($SM_{hydrous}$ ~30-35 in Fig. 4), whereas, for more depolymerized liquids ($SM_{hydrous}$ >30-35) it tends to level off and not to be affected by the introduction of H_2O (Fig. 2) or others oxides (Fig. 4). This general trend seems not to include An_{10} composition and the tephritic and NIQ compositions from Bouhifd (2013), which instead display a small but distinctive increase of C_p^c as H_2O is introduced into the liquid. In contrast, the Etna compositions display the opposite behavior with a small increase in C_p^c upon introduction of H_2O. The limited number of calorimetric data for hydrous melts and, in particular, on melts having very high H_2O contents (e.g., >10 mol %) precludes an unambiguous interpretation of this behavior.

In deriving $SM_{hydrous}$ and $NBO/T_{hydrous}$ parameters, we consider total H_2O to be a network modifier without accounting for water speciation, therefore possibly overestimating the extent of H_2O in a network modifier role. Speciation of water and the different structural role of molecular versus hydroxyl groups are therefore fundamental to specifically address this issue. Moreover, the presence of H_2O may influence the oxidation state of iron (Fe^{2+}/Fe^{3+}) affecting the calculation of the considered polymerization parameter, which in this case have been set on the basis of the structural considerations provided by Mercier et al. (2009) to $Fe^{2+/}Fe^{3+}$ = 0.5.

In summary whereas general trends can be envisaged in both C_p^c and C_p^g as a function of chemical compositions and degree of depolymerization, further data exploring the complexity of natural melts is required in the future to validate and generalize our modeling and interpretation. At present, there are insufficient experimental data to model the effect of iron redox on the heat capacities of multicomponent silicate melts, so also in this case, further studies will be needed to investigate this aspect more in details. Finally, our approach is strictly empirical; the chemical components we have chosen have no explicit or independent relationship to the structure or speciation of the silicate melt. We believe that future models may benefit immensely from a calibration based on a component basis that, at least in part, reflects melt speciation.

5. Conclusions.

The results of this investigation show that:

1) the C_p of polymerized and depolymerized compositions are different and can be largely distinguished in terms of compositional parameters accounting for the modifying effect of H_2O in the structure (e.g., $SM_{hydrous}$ or NBO/T);

2) a compositional dependence of the partial molar heat capacity of H_2O for both glasses and liquids has not been observed;

3) we estimate an optimal $C_p{}^l{}_{H2O}$ of 79 J mol^{-1} K^{-1};

4) our value for $C_p{}^l{}_{H2O}$ used in conjunction with existing predictive models for anhydrous melts can reproduce measured C_p values for hydrous glasses and liquids to within 3% relative error;

5) the Adam-Gibbs equation fitted to a large dataset comprising the corresponding measurements of melt viscosity constrains the high temperature limits of melt viscosity $10^{-3.5}$ Pa s and provides estimates of B_{AG} and $S^c{}_{AG}$;

6) values of B_{AG} and $S^c{}_{AG}$ strongly reflect the degree of polymerization of the melts and are strongly affected by H_2O content of the melt.

It is possible that the absence of a distinct temperature or compositional dependence of $C_p{}^l{}_{H2O}$ observed in our study could indeed reflect an incomplete sampling of the wide range of chemical composition pertaining to natural systems. Apart from Etna trachybasalt, all the data shown in Fig 4 derive from simplified synthetic systems. It should also be noted that none of the models presented here account for the partitioning of H_2O species into the silicate liquids or for their possible interactions with the other oxide components. In addition, we have treated iron as a single species (FeO_{tot}), whereas silicate melts contain both ferric and ferrous iron and their proportions, which can vary according to temperature, composition and H_2O content, and can substantially affect the structure of the melt (Mysen, 1988; Dingwell, 1991), but probably not their physical properties (Chevrel et al. 2013).

Finally, we believe that new models should be recalibrated using measurements obtained on multicomponent anhydrous and hydrous liquids that consider how H_2O species partition into the melt structure, how H_2O species interact with other oxide components, and the redox state of iron.

Acknowledgments.

The authors would like to knowledge two anonymous reviewers for constructive comments that have led to clarification of the initial manuscript. JKR acknowledges financial support for this research from grants awarded through the NSERC Discovery and Discovery Accelerator Supplements programs.

References

Adam G, Gibbs JH (1965) On the temperature dependence of cooperative relaxation properties in glass-forming liquids. J Chem Phys 43,139–146

Avramov I (2013) The role of entropy on viscosity of silicates. J Non-Crystalline Solids 362:120-123.

Behrens H, Romano C, Nowak M, Holtz F, Dingwell DB (1996) Near infrared spectroscopic determination of H2O species in glasses of the system $MAlSi_3O_8$ (M = Li, Na, K): an interlaboratory study. Chem Geol 128, 41-63;

Behrens H, A Stuke (2003) Quantification of H_2O contents in silicate glasses using IR spectroscopy-a calibration based on hydrous glasses analyzed by Karl-Fisher tritation Glass Sci. Tech. 76, 176-189;

Bouhifd MA, Whittington A, Roux J, Richet P (2006) Effect of H_2O on the heat capacity of polymerized aluminosilicate glasses and melts. Geochim Cosmochim Acta 70, 711–722;

Bouhifd MA, Whittington A, Withers AC, Richet P (2013) Heat capacities of hydrous silicate glasses and liquids Chem Geol 346, 125 - 134;

Bowen NL (1915) The crystallization of haplobasaltic, haplodioritic and related magmas Am J Sci 40, 161-185;

Burnham CW, Davis NF (1974) The role of H_2O in silicate melts: II Thermodynamic and phase relations in the system $NaAlSi_3O_8$ - H_2O to 10 kilobars, 700 - 1000 ºC Am Jour Sci 274, 902 - 940;

Chevrel MO, Giordano D, Potuzak M, Courtial P, Dingwell DB (2013) Physical properties of $CaAl_2Si_2O_8$ - $CaMgSi_2O_6$ - FeO - Fe_2O_3 melts: Analogues for extra-terrestrial basalt Chem Geol 346, 93 - 105;

Clemens JD, Navrotsky A (1987) Mixing properties of $NaAlSi_3O_8$ melt-H_2O: new calorimetric data and some geological implications J Geology 95, 173 - 186;

Courtial P, Richet P (1993) Heat capacity of magnesium aluminosilicate melts Geochim Cosmochim Acta 57, 1267–1275;

Di Genova D, Romano C, Giordano D, Alletti M (2014) Heat capacity, configurational heat capacity and fragility of hydrous magmas Geochim Cosmochim Acta 142, 314 - 333;

Di Muro A, Metrich N, Mercier M, Giordano D, Massarre D, Montagnac G (2009). MicroRaman Determination of Iron Redox State in Dry Natural Glasses: Application to Peralkaline Rhyolites and Basalts. Chem. Geol., 259, 78-88;

Dingwell DB (1991) Redox viscometry of some Fe-bearing silicate melts Am Mineral 76, 1560–1562;

Fulcher GS (1925) Analysis of recent measurements of the viscosity of glasses Am Ceramic Soc J 8:339-355

Ghiorso MS, Sack RO (1995) Chemical mass transfer in magmatic processes: IV A revised and internally consistent thermodynamic model for the interpolation and extrapolation of liquid-solid equilibria in magmatic systems at elevated temperature and pressures Contrib Mineral Petrol.119, 197-212.

Giordano D, Dingwell DB (2003) Viscosity of hydrous Etna basalt: implications for Plinian-style basaltic eruptions Bull Volcanol 65, 8-14;

Giordano D, Nichols, ARL, Dingwell DB (2005) Glass transition temperatures of natural hydrous melts: a relationship with shear viscosity and implications for the welding process J Volcanol Geoth Res 142, 105–118;

Giordano D, Russell JK (2007) A rheological model for glassforming silicate melts in the systems CAS, MAS, MCAS J Phys Cond Matter 19, 205148

Giordano D, Potuzak M, Romano C, Dingwell DB, Nowak M (2008a) Viscosity and glass transition temperature of hydrous melts in the system $CaAl_2Si_2O_8$ - $CaMgSi_2O_6$ Chem Geol 256, 203-215;

Giordano D, Russell J.K, Dingwell DB (2008b) Viscosity of magmatic liquids: A model Earth Planet Sci Lett 271, 123-134

Giordano D, Ardia P, Romano C, Dingwell DB, Di Muro A, Schmidt MW, Mangiacapra A, Hess KU (2009) The rheological evolution of alkaline Vesuvius magmas and comparison with alkaline series from the Phlegrean Fields, Etna, Stromboli and Teide Geochim Cosmochim Acta 73, 6613–6630;

Kress VC, Carmichael ISE (1991) The compressibility of silicate liquids containing Fe_2O_3 and the effect of composition, temperature oxygen fugacity and pressure on their redox states Contrib Mineral Petrol 108, 82–92;

Knoche R (1993) Temperaturabhängige Eigenschaften silikatischer Schmelzen Untersuchungen in den Systemen Na2O-SiO2 und $NaAlSi_3O_8$ - $CaAl_2Si_2O_8$ - $CaMgSi_2O_6$ Dissertation, Universität Bayreuth 186 pp;

Kushiro I (1973) The system diopside-anorthite-albite: determination of compositions of coexisting phases Carnegie Inst Washington Year book 72, 502-507;

Lange RA, Navrotsky A (1992) Mineralogy and Heat capacities of Fe_2O_3-bearing silicate liquids Contrib Mineral Petrol 110, 311 - 320;

Maier CG, Kelley KK (1932) An equation for the representation of high temperature heat content data J Am Ceramic Soc 54, 3243-3345;

Mercier M, Muro A D, Giordano D, Metrich N, Lesne P, Pichavant M, Scaillet B, Clocchiatti R, Montagnac G (2009) Influence of glass polymerization and oxidation on micro-Raman H_2O analysis in alumino-silicate glasses Geochim Cosmochim Acta 73, 197–217;

Moynihan CT (1995) Structural relaxation in the glass transition In: Stebbins J.F, McMillan P.F, Dingwell D.B (Eds), Structure, Dynamics and Properties of Silicate Melts Reviews in Mineralogy, 32, Mineralogical Society of America, Washington, D.C, pp 1-19;

Mysen BO (1988) Structure and properties of Silicate Melts Elsevier Publishing Company, Amsterdam;

Navrotsky A, Hon R, Weill DF, Henry DJ (1980) Thermochemistry of glasses and liquids in the system $CaMgSi_2O_6$ - $CaAl_2Si_2O_8$ - $NaAlSi_3O_8$, SiO_2-$CaAl_2Si_2O_8$-$NaAlSi_3O_8$ and SiO_2-Al_2O_3-CaO-Na_2O Geochim Cosmochim Acta 44, 1409-1423;

Navrotsky A (1995) Energetics of Silicate Melts Rev Mineral 32, 121-143;

Perugini D, Poli G (2005) Viscous Fingering During Replenishment of Felsic Magma Chambers by Continuous Inputs of Mafic Magmas: Field Evidence and Fluid-Mechanics Experiments, Geology 33, 5-8.

Potuzak M, Nichols ARL, Dingwell DB, Clague DA (2008) Hyperquenched volcanic glass from Loihi Seamount, Hawaii, Earth and Planetary Science Letters 270 (1), 54-62

Pyle DM (1995) Mass and energy budgets of explosive volcanic eruptions Geophys Res Lett 22, 563-566;

Press WH, Flannery BP, Teukolsky SA, Vetterling WT (1986) Numerical Recipes: the Art of Scientific Computing Cambridge University Press, Cambridge, 818 p.

Richet P (1987) Heat capacity of silicate glasses Chem Geol 62, 111–124;

Richet P (1984) Viscosity and configurational entropy of silicate melts: Geochim Cosmochim Acta 48, 471–483;

Richet P, Bottinga Y (1985) Heat capacity of aluminum-free liquid silicates Geochim Cosmochim Acta 49, 471–486;

Richet P, Neuville DR (1992) Thermodynamics of silicate melts: Configurational properties In (Ed S Saxena) Advances in Physical Geochemistry 10:132-161

Richet P, Bottinga Y (1995) Rheology and Configurational Entropy of Silicate Melts In Structure, Dynamics and Properties of Silicate Melts, (Eds J.F Stebbins, P.F McMillan and Dingwell DB), Rev Mineral 32, 67-94;

Russell JK (1990) Magma Mixing Processes: Insights and constraints from thermodynamics calculations In Modern Methods of Igneous Petrology: Understanding Magmatic Processes (Eds J Nicholls, J.K Russell), Rev Mineral 24, 153 - 190;

Russell JK, Giordano D, Dingwell DB, Hess KU (2002) Modelling the non-Arrhenian rheology of silicate melts: Numerical considerations Eur J Min 14, 417–427

Russell JK, Giordano D, Dingwell DB (2003) High-temperature limits of non-Arrhenian silicate melts: Implications for modelling compositional dependencies Am. Min. 88, 1390-1394;

Russell JK, Giordano D (2005) A model for silicate melt viscosity in the System CaMgSi2O6-$CaAl_2Si_2O_8$-$NaAlSi_3O_8$ Geochim Cosmochim Acta 69, 5333-5349;

Sahagian DI, Proussevich AA (1996) Thermal effects of magma outgassing Jour Volcanol Geoth Res 74, 19 - 38;

Stebbins JF, Carmichael, I.S.E, and Moret, L.K (1984) Heat capacities and entropies of silicate liquids and glasses Contrib Mineral Petrol 86, 131–148;

Toplis MJ (1998) Energy barriers to viscous flow and the prediction of glass transition temperatures of molten silicates Am Min 83, 480–490;

Toplis MJ, Dingwell DB, Hess KU, Lenci T (1997) Viscosity, fragility and configurational entropy of melts along the join SiO_2-$NaAlSiO_4$ Am Min 82, 979–990;

Toplis MJ, Gottsmann J, Knoche R, Dingwell DB (2001) Geochim Cosmochim Acta 65, 1985-199;

Webb SL (2008) Configurational heat capacity of Na_2O–CaO–Al_2O_3–SiO_2 melts Chem Geol 256, 92–101

Weill DF, Hon R, Navrotsky A (1980) The igneous system $CaMgSi_2O_6$ - $CaAl_2Si_2O_8$ -$NaAlSi_3O_8$: variations on a classic theme by Bowen In: Hargraves R.B (eds) Physics of Magmatic Processes Princeton University Press, Princeton, 49-92;

Whittington AG, Bouhifd MA, Richet P (2009) The viscosity of hydrous $NaAlSi_3O_8$ and granitic melts: Configurational entropy models Am Min 94:1-16

Captions to Figures

Figure 1. The heat capacity curve (C_p) from DSC experiment on glass An_{42} showing how T_g^{onset}, T_g^{peak} and T_g^{liquid} are defined. The Cp curve in the figure was generated after cooling and heating from the glassy state through the glass transition at 10 K/min. A successful measurement is indicated by the glass returning to the same value of C_p after each cooling (not shown here). The dashed line is the Maier Kelley (MK) fit to the glass heat capacity.

Figure 2. Variation of C_p^g, (triangles) C_p^l (circles) and C_p^c (squares) as a function of H_2O content in variably hydrated (a) Etna trachybasalt (Giordano and Dingwell, 2003; Giordano et al. 2005) and (b) melts in the An-Di system. Lines in both panels define $c_p^i = c_p{}^i{}_{\mathrm{dry}} + a^i\, H_2O + b^i\, H_2O^2$ fitted to each of the Etna trachybasalt C_p datasets allowing direct comparison with glasses and melts in the An - Di system in (b).

Figure 3. Values of C_p^g (triangles), C_p^l (circles) and C_p^c (squares) for all samples (Table 1) plotted as a function of (a) $SM_{hydrous}$ and (b) $NBO/T_{hydrous}$. Symbols are as in Figure 2. Values of C_p^g and C_p^l show a general decrease with increasing depolymerization, i.e., increasing $SM_{hydrous}$ and $NBO/T_{hydrous}$. In particular, the more polymerized compositions of the An-Di system (An_{100}, An_{90}) have higher C_p^g and C_p^l than Etna trachybasalt that in turn have higher C_p^g and C_p^l and are more depolymerized than An_{42} and An_{90}. Absolute variations of C_p^c are also shown and can correspond to as much as 20 % relative (see text).

Figure 4. Variation of C_p^g (triangles), C_p^l (circles) and C_p^c (squares) shown as a function of (a) H_2O (mol%) and (b) $SM_{hydrous}$ for samples measured here (Fig. 3) combined with the measurements of Bouhifd et al (2006). (a) Data plotted to show the effect of H_2O on the C_p of the more depolymerized melt tefritic compositions (Teph, NIQ; Bouhifd et al. 2013). The overall effect of H_2O on C_p of these depolymerized compositions is similar to that shown for the Etna trachybasalts. (b) Inclusion of the literature data allows C_p variations to be examined over a much wider range of $SM_{hydrous}$ values than has previously been possible. Largely, more polymerized melts have lower C_p^l and C_p^c, and higher C_p^g than depolymerized natural melts. C_p^c increases at low $SM_{hydrous}$ values until becoming constant at >35 mol%. C_p^l and C_p^g appear to show apparent minima at SM values of 45 (see text).

Figure 5. Measured and modelled glass transition temperatures for silicate melts for which hydrous heat capacity data exist, including data reported here and data compiled from the literature (Table 2). (a) T_g^{liquid} (K) against T_g^{onset} (K) for the fully relaxed melt defined using C_p curves (Fig. 1); compiled data are from Giordano et al (2005, 2008), Bouhifd et al (2006, 2013) (Table 1). All data plot above the 1:1 model line and can be modelled by an offest temperature of 57.5 K. (b) T_g (K) values taken as the temperature at which $\eta = 10^{12}$ Pa s as predicted by temperature dependent viscosity curves (e.g., Eq. 1; see text and Appendix) plotted against T_g^{onset} (K).

Figure 6. Calculated fitting parameters for the Adam-Gibbs temperature dependent equation (Eqs. 1, 2) for melt viscosity to thermochemical and viscosity datasets for melt compositions listed in Table 2. (a) Best estimate values returned for adjustable parameters B_{AG} and $S^c(T_g)$ for 41 anhydrous (black symbols) and hydrous (grey symbols) melt compositions assuming a common but unknown high temperature limiting viscosity (*A*). The global fit uses 23 melts to constrain the value of *A* to -3.51 (black symbols); 18 other melts having fewer viscosity measurements were fit for values of *B* and $S^c(T_g)$ assuming this same optimal value of *A* (grey symbols). Symbol sizes of hydrous melts are proportional to water content. (b) Measured values of log η plotted against predicted values calculated with the optimal value of *A* and values of B_{AG} and $S^c(T_g)$ obtained for individual melt compositions. Dashed lines denote +/- 0.25 log units. Symbols as in (a). (c) Derivative melt properties, including glass transition temperature (Tg^{12}) and melt fragility (*m*), calculated from the model (Table 2) for anhydrous (black) and hydrous (grey) melts (see text); symbol size is proportional to water contents.

Figure 7. Covariation of the $B_{AG}/S^c(T_g)$ ratio with melt composition as expressed by the variables (a) H_2O *mol%* and (b) $SM_{hydrous}$.

Figure A1. The 1σ solution space for the Adam-Gibbs equation fitted to each of the datasets Ab, Jd, and Ne (Table A1). The confidence envelopes on the solution are shown as 2-D slices through the corresponding 3-D confidence ellipsoid. The plane through the 3-D ellipsoid is chosen to contain the solution and be parallel to one of the parameters *A*, *B* and S^c making it a constant in that space (see text). (A) *A*-*B* plane; (B) *A*- S^c plane; and (C) *B*- S^c plane.

Figure A2. The entire Ab-Jd-Ne dataset (N=36) is fit to the Adam-Gibbs equation assuming that all three melt compositions share a common (but unknown) value of *A* and individual values of *B* and S^c. Main figure compares the 1σ confidence ellipses (dotted lines) on the optimal values of *B* and S^c (solid circles) for each melt composition at the model value of *A* (-3.80 ± 2.2). Inset shows the level of misfit in values of log η predicted from the global optimization. Dashed lines denote ±0.25 log units of viscosity.

Figure A3. Comparison of model curves for temperature dependent viscosity and measured data for Ab, Jd, and Ne melts (Table A1). The viscosity, C_p^c, and T_g (K) datasets for each melt composition are fit simultaneously to model Adam-Gibbs curves (Eq. A3) assuming that there is a single common value of *A* (–3.8). The shaded fields are the 1σ confidence limits for the model functions derived from the confidence ellipses shown in Figure A2.

Figure A4. Estimates of S^c (T_g) for three silicate melts (Ab, Jd, Ne) plotted against composition represented by SiO_2 content (mol. %). The original results of Toplis et al. (1997) are reproduced here (cf. their Fig. 8b) and compared to the estimates obtained in this work where we assume the three melts share a common value of *A*.

REVISED_FIGURES

Click here to download Figure: Giordano_et_al_REVISED_FIGURES.pdf

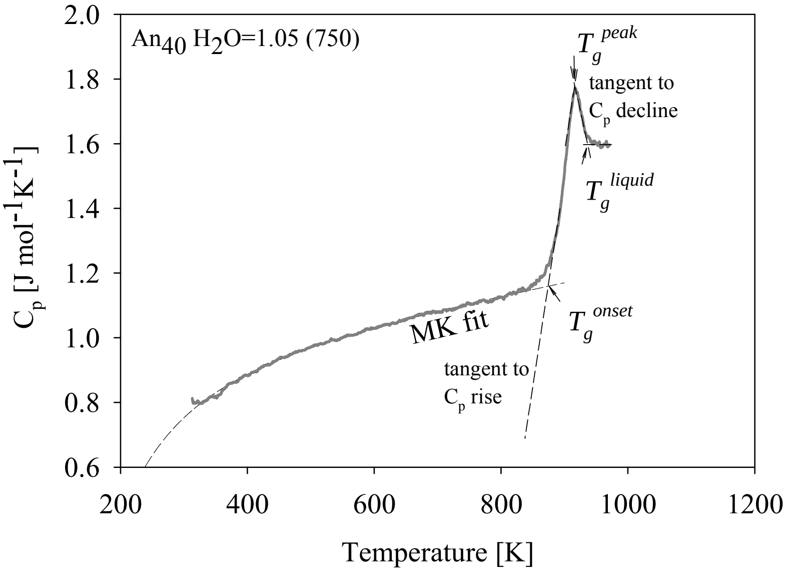

Figure 1. Giordano et al. (2015) [CMP]

Figure 2 Giordano et al. (2015) [CMP]

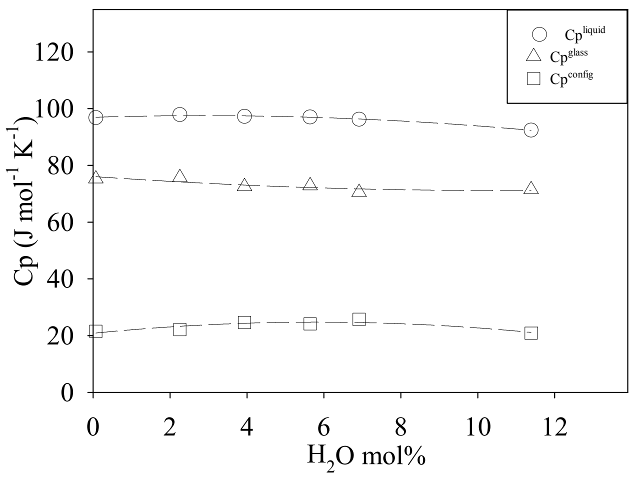

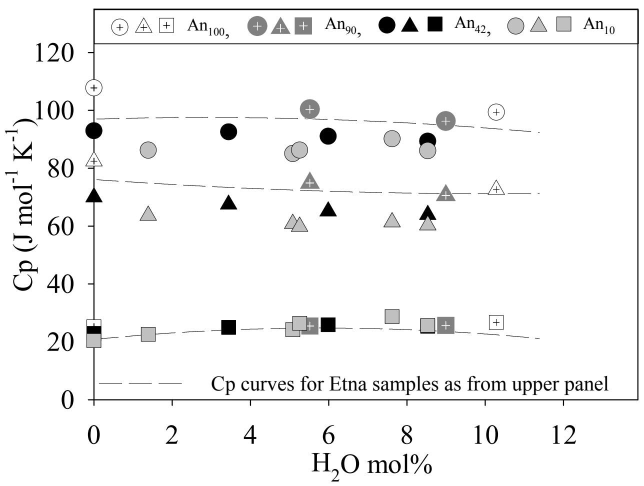

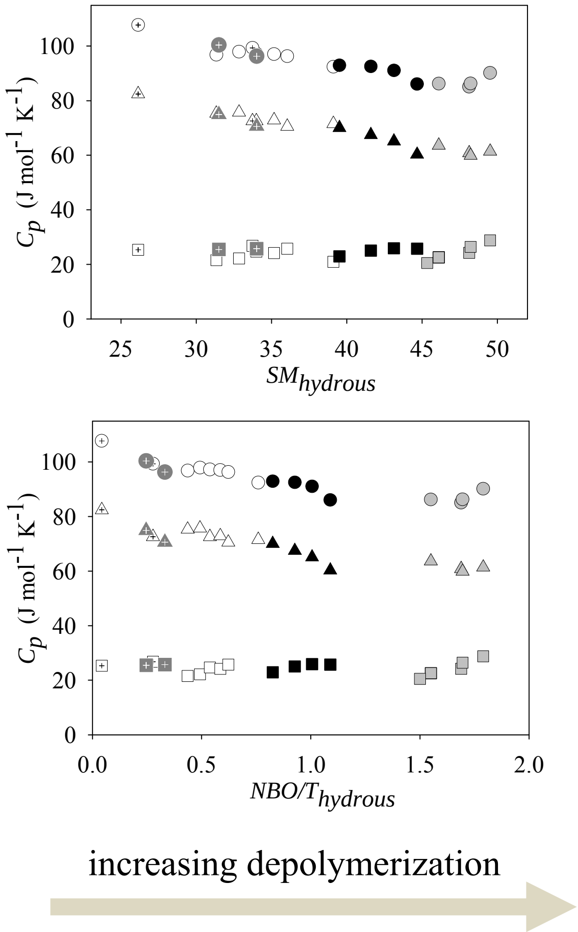

Figure 3. Giordano et al. (2015) [CMP]

Figure 4. Giordano et al. (2015) [CMP]

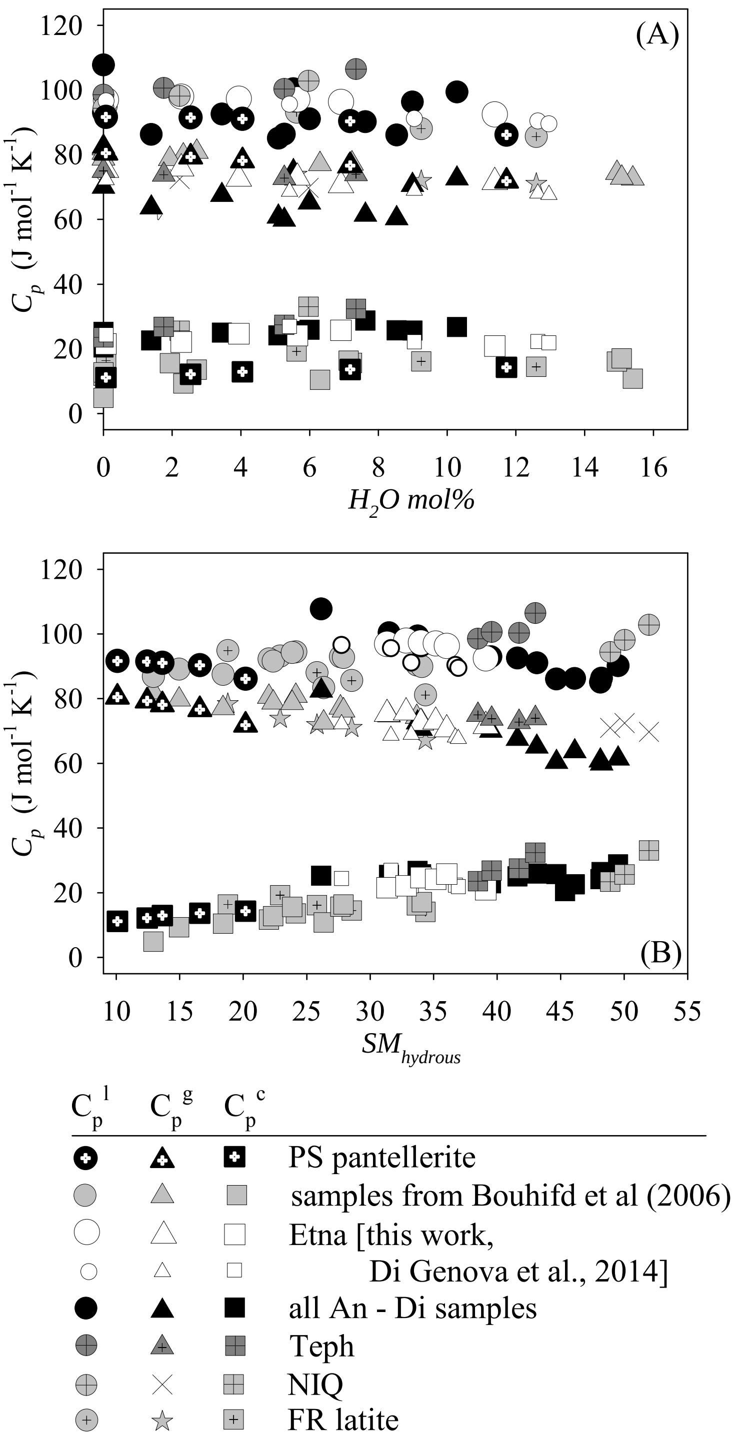

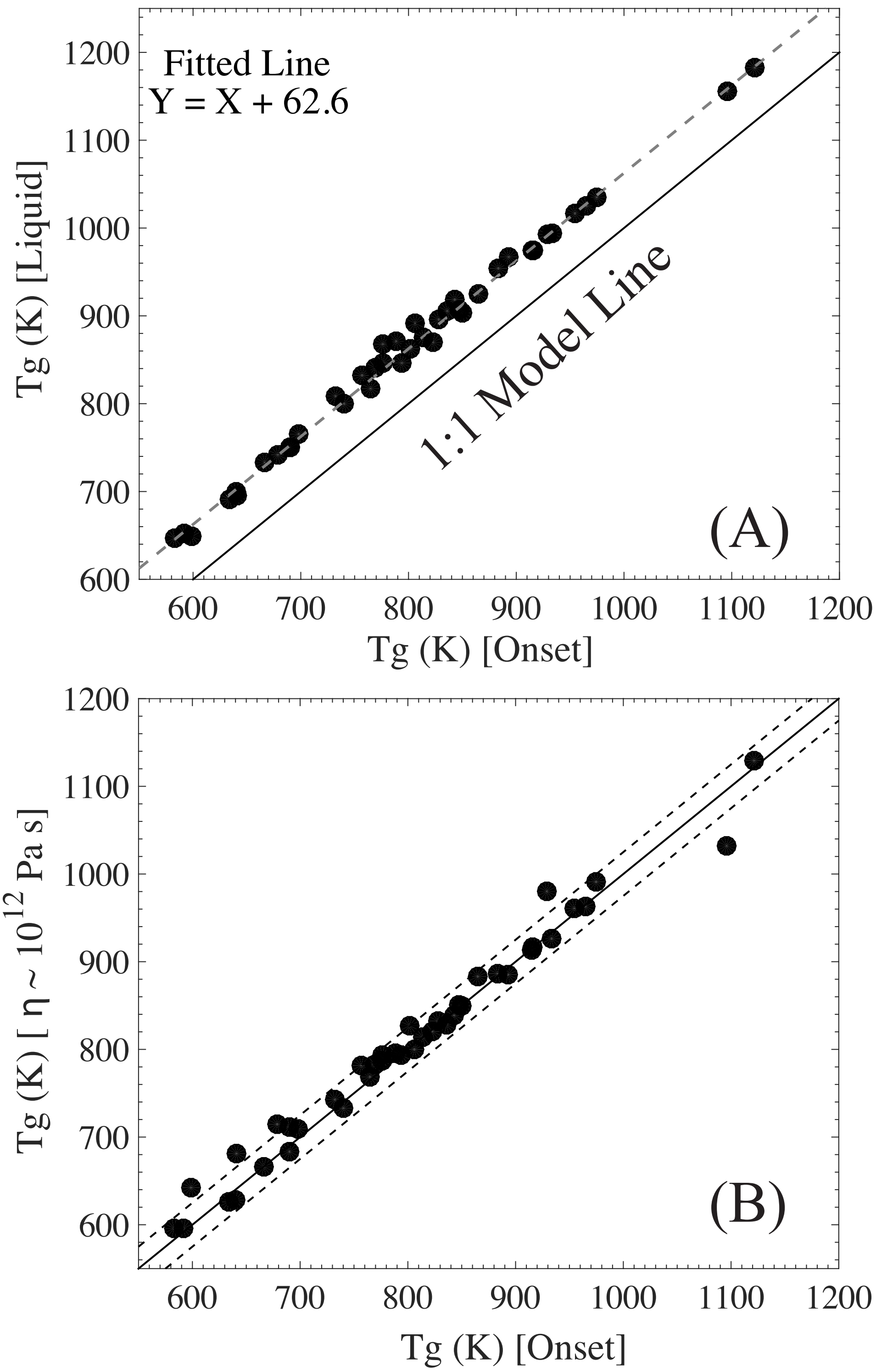

Figure 5. Giordano et al. (2014) [CMP]

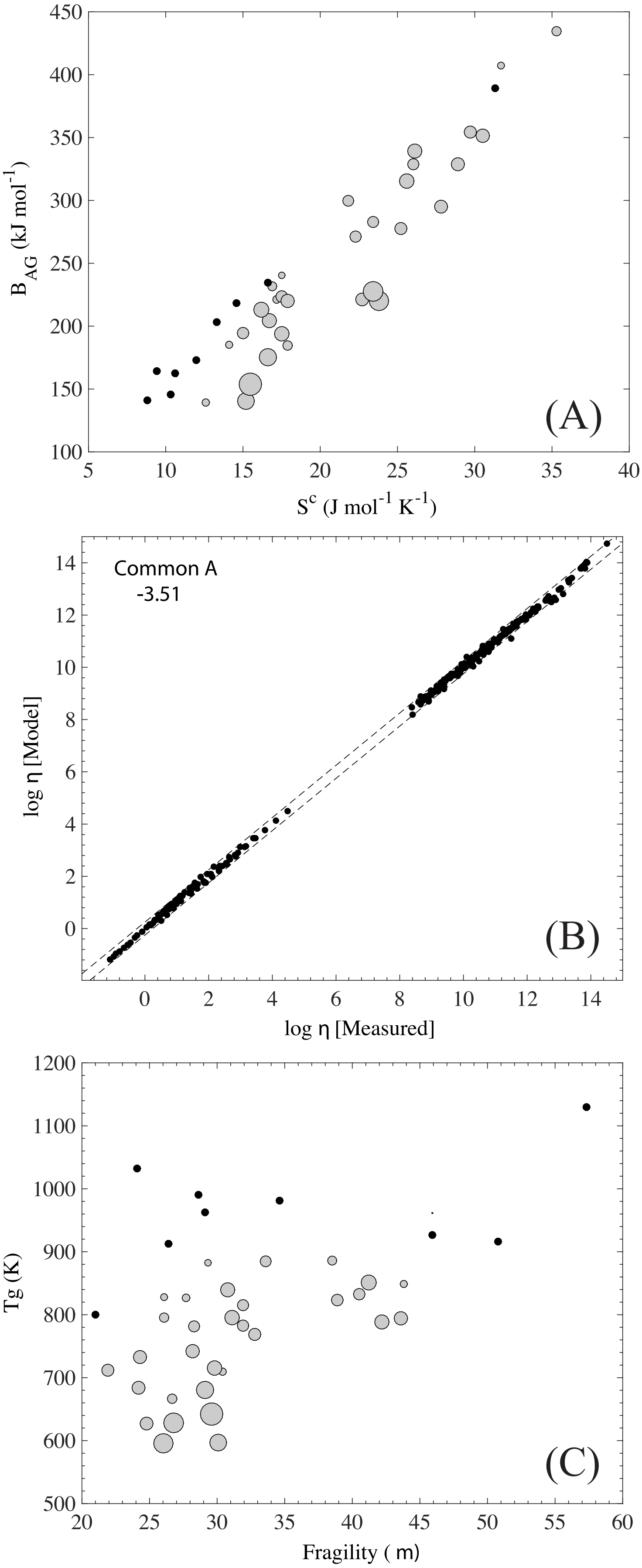

Figure 6. Giordano et al. (2014) [CMP]

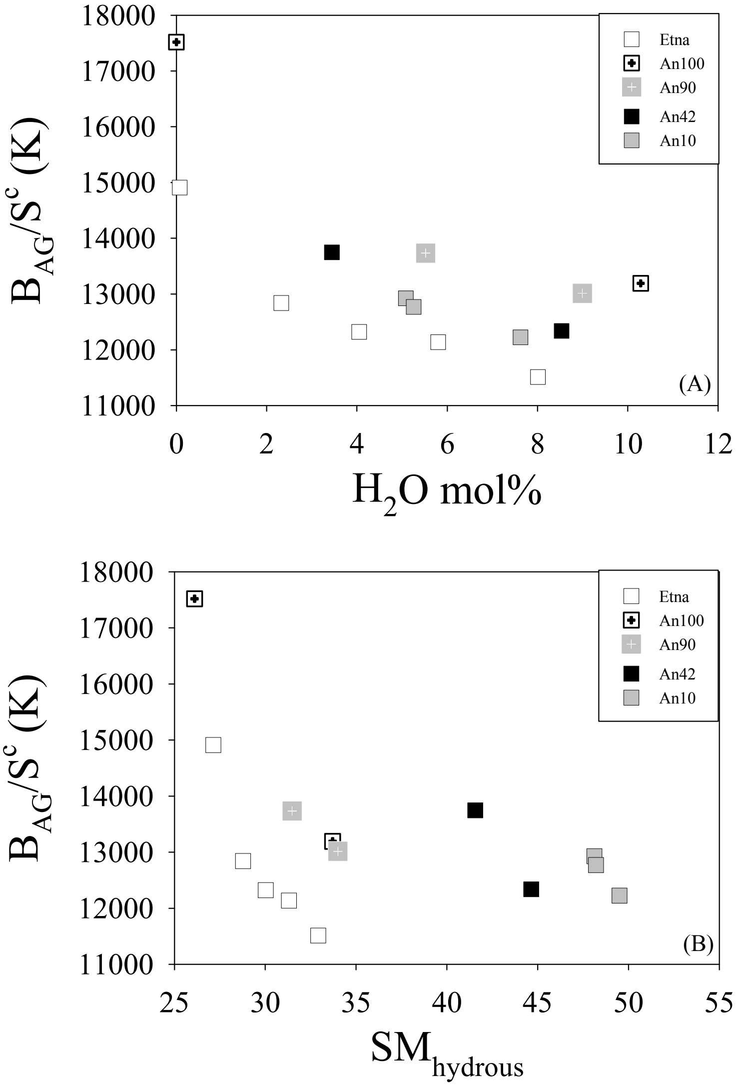

Figure 7. Giordano et al. (2015) [CMP]

REVISED_TABLES

Click here to download Table: Giordano_et_al_REVISED_TABLES.pdf

Table 1. Experimentally measured compositional and thermochemical properties of anhydrous and hydrous melts and calculated compositional parameters (SM, NBO/T). Measurements include onset and liquid glass transition temperature (Tg^{onset} and Tg^{liquid}) and the glass, liquid and configurational heat capacities (Cp^g, Cp^l and Cp^c) observedat heating rates of 10 K/min. Measured values of Cp^l are compared to values predicted L&N'92, RBC and S'84 models for different va

	H_2O	H_2O	SM	NBO/T	Tg^{onset}	Tg^{liquid}	Cp^g	Cp^l	Cp^c	L&N '92	dev%	RBC	dev%	S '84	dev%	L&N '92	dev%	RBC	dev%	S '84	dev%	L&N '92	dev%	RBC	dev%	S '84	dev%
										Calculated Cp liquid using various models with variable Cp_{H2O}																	
	wt%	mol%			(K)	(K)		$J\ mol^{-1}\ K^{-1}$		$Cp_{H2O} = 79\ J\ mol^{-1}\ K^{-1}$						$Cp_{H2O} = 85\ J\ mol^{-1}\ K^{-1}$						$Cp_{H2O} = 257\ J\ mol^{-1}\ K^{-1}$					
Etna (trachybasalt)	0.02	0.074	27.14	0.465	954	1017	73.54	94.59	21.05	98.52	3.68	95.46	1.08	97.49	2.64	98.53	4.02	95.47	1.17	97.49	2.98	98.64	12.73	95.58	9.67	97.61	11.69
801 [1]	0.64	2.324	28.78	0.526	836	905	74.03	95.69	21.66	98.08		95.03		97.07		98.22		95.17		97.21		101.76		98.71		100.74	
800 [1]	1.13	4.050	30.04	0.574	776	868	70.94	95.08	24.15	97.75		94.79		96.75		97.99		95.03		97.00		104.15		101.19		103.15	
BET 1-3	1.64	5.801	31.31	0.625	769	841	71.28	94.90	23.62	97.41		94.51		96.43		97.75		94.86		96.78		106.57		103.68		105.60	
802 [1]	2.31	8.011	32.92	0.692	732	809	68.36	93.33	24.97	96.97		94.21		96.02		97.45		94.69		96.50		109.66		106.90		108.71	
803 [1]	3.46	11.689	35.61	0.811	708	788	70.03	90.52	20.48	96.25		93.66		95.34		96.96		94.36		96.04		114.72		112.12		113.81	
ETN DRY	0.02	0.076	27.75	0.405	909	-	72.20	96.60	24.40	100.83	10.81	97.35	7.20	99.56	9.45	100.83	11.36	97.35	7.75	99.57	10.00	100.96	27.14	97.48	23.52	99.70	25.78
ETN 1.4	1.48	5.412	31.64	0.548	769	858	68.60	95.60	27.00	99.80		96.51		98.60		100.12		96.84		98.93		109.43		106.15		108.24	
ETN 2.9	2.40	9.045	33.24	0.647	707	-	68.90	91.10	22.20	102.71		98.64		101.25		103.25		99.19		101.79		118.81		114.74		117.35	
ETN 3.6	3.67	12.639	36.72	0.756	656	-	68.10	90.40	22.30	98.03		95.27		96.91		98.79		96.03		97.67		120.53		117.76		119.41	
ETN 3.8	3.76	12.966	36.94	0.769	655	-	67.60	89.50	21.90	98.27		95.52		97.15		99.05		96.30		97.93		121.35		118.60		120.23	
An100	0.00	0.000	26.11	0.043	1122	1183	82.42	107.71	25.29	105.59	3.46	103.98	1.90	103.96	3.90	105.59	3.72	103.98	1.91	103.96	4.21	105.59	11.99	103.98	8.83	103.96	12.77
An100	2.90	10.287	33.71	0.277	847	907	72.59	99.34	26.75	102.86		99.30		101.39		103.48		99.92		102.01		119.11		115.56		117.65	
An90Di10	1.53	5.522	31.49	0.246	893	967	74.88	100.37	25.48	102.39		99.03		101.13		102.72		99.36		101.46		111.12		107.76		109.86	
An90Di10	2.56	8.994	34.00	0.332	843	918	70.57	96.29	25.72	101.53		97.94		100.32		102.07		98.48		100.86		115.74		112.15		114.53	
An42Di58	0.00	0.000	39.48	0.826	1009	1070	70.04	92.93	22.89	95.12		91.91		95.86		95.12		91.91		95.86		95.12		91.91		95.86	
An42Di58	1.05	3.445	41.57	0.927	883	954	67.50	92.52	25.02	94.57		91.02		95.28		94.78		91.22		95.48		100.01		96.46		100.72	
An42Di58	1.86	5.990	43.11	1.007	840	916	65.13	91.04	25.90	94.16		90.55		94.85		94.52		90.91		95.21		103.62		100.02		104.31	
An42Di58	2.70	8.533	44.65	1.090	788	871	60.31	86.03	25.72	93.75		90.07		94.42		94.26		90.58		94.93		107.23		103.55		107.90	
An10Di90	0.00	0.000	45.34	1.501	1003	1047	0.00	0.00	20.49																		
An10Di90	0.45	1.389	46.10	1.550	942	1010	63.62	86.22	22.61	88.80		85.40		90.75		88.89		85.48		90.83		91.00		87.59		92.94	
An10Di90	1.69	5.084	48.12	1.689	828	896	60.83	85.06	24.23	88.44		85.06		90.31		88.74		85.37		90.61		96.47		93.10		98.34	
An10Di90	1.75	5.258	48.22	1.695	822	870	59.87	86.29	26.42	88.42		85.05		90.29		88.73		85.36		90.60		96.73		93.36		98.60	
An10Di90	2.58	7.623	49.51	1.790	777	846	61.41	90.17	28.76	88.18		84.86		90.01		88.64		85.32		90.46		100.23		96.90		102.05	
HAB0	0.00	0.000	12.93	0.114	1096	-	81.99	86.84	4.85	91.13	4.34	90.47	2.75	88.74	2.04	91.13	4.73	90.47	3.17	88.74	2.39	91.13	15.47	90.47	13.92	88.74	12.89
HAB0.6	0.67	2.323	14.95	0.165	815	-	79.74	89.09	9.35	90.85		89.46		88.52		90.99		89.60		88.66		94.52		93.13		92.19	
HAB2.2	1.87	6.297	18.41	0.256	690	-	77.04	87.49	10.45	90.37		88.72		88.13		90.74		89.10		88.51		100.31		98.67		98.08	
HAB5.2	4.91	15.403	26.34	0.499	602	-	72.58	83.41	10.83	89.26		87.58		87.24		90.19		88.50		88.17		113.60		111.92		111.58	
Phon 0.	0.00	0.000	22.02	0.327	915	*975*	80.55	92.23	11.68	92.64	1.77	89.62	3.93	90.90	2.50	92.64	1.17	89.62	3.53	90.90	2.10	92.64	10.01	89.62	8.72	90.90	8.96
Phon 0.5B	0.78	2.712	24.13	0.392	802	*862*	80.82	94.41	13.59	92.27		89.18		90.57		92.44		89.34		90.74		96.56		93.46		94.86	
Phon 2.2	2.15	7.229	27.66	0.508	690	*750*	77.25	92.92	15.67	91.66		88.64		90.04		92.09		89.08		90.47		103.08		100.07		101.46	
Phon 5	4.72	14.944	33.67	0.736	592	*652*	74.33	90.39	16.06	90.61		87.90		89.12		91.50		88.80		90.02		114.22		111.51		112.73	
Trach =.	0.00	0.000	22.36	0.380	965	*1025*	78.80	91.59	12.79	90.88	2.90	88.45	3.88	89.64	2.70	90.88	1.74	88.45	3.57	89.64	2.38	90.88	9.05	88.45	7.30	89.64	7.30
Trach 50	0.57	1.930	23.85	0.427	865	*925*	78.63	94.22	15.59	90.65		88.12		89.43		90.77		88.23		89.55		93.70		91.17		92.48	
Trach2.2	2.19	7.136	27.90	0.563	740	*800*	76.35	92.71	16.36	90.03		87.49		88.88		90.46		87.92		89.31		101.31		98.77		100.15	
Trach5	4.92	15.081	34.07	0.803	640	*700*	72.83	89.90	17.07	89.09		86.71		88.03		89.99		87.62		88.94		112.92		110.54		111.86	
tephdry	0.00	0.000	38.49	0.861	933	*994*	74.96	98.50	23.54	94.50	6.12	92.03	8.25	94.86	5.74	94.50	5.95	92.03	8.09	94.86	5.58	94.50	2.40	92.03	3.86	94.86	2.16
teph0.3	0.52	1.754	39.57	0.912	878	*938*	73.79	100.60	26.81	94.23		91.87		94.58		94.34		91.97		94.69		97.00		94.64		97.35	
teph1.5	1.60	5.260	41.73	1.020	814	*875*	72.81	100.30	27.49	93.69		91.54		94.03		94.00		91.86		94.34		102.00		99.85		102.34	
teph2.2	2.27	7.348	43.01	1.088	794	*847*	73.98	106.40	32.42	93.36		91.32		93.69		93.81		91.76		94.14		104.97		102.93		105.30	
NIQ 0	0.00	0.000	48.90	1.508	916	*975*	71.03	94.39	23.36	93.11	5.68	91.45	7.04	95.18	4.19	93.11	5.52	91.45	6.88	95.18	4.03	93.11	1.44	91.45	2.80	95.18	0.61
NIQ 0.6	0.68	2.216	50.03	1.587	850	*903*	72.47	98.13	25.66	92.80		91.40		94.82		92.93		91.53		94.95		96.30		94.90		98.32	
NIQ 1.8	1.88	5.963	51.95	1.730	765	*818*	69.78	102.80	33.02	92.27		91.34		94.21		92.63		91.70		94.57		101.69		100.77		103.63	
PS DRY	0.02	0.072	10.10	0.099	806	892	80.50	91.60	11.10	82.5272	8.47	80.41	10.71	80.17	10.97	82.5315	8.13	80.42	10.37	80.17	10.62	82.65	8.20	80.54	8.69	80.29	8.74
PS 0.5	0.72	2.536	12.44	0.158	698	766	79.30	91.50	12.20	82.6639		80.60		80.36		82.816		80.75		80.52		87.18		85.11		84.88	
PS 1.1	1.16	4.040	13.63	0.191	666	733	78.10	91.00	12.90	82.4513		80.39		80.18		82.6938		80.64		80.42		89.64		87.59		87.37	
PS 2.2	2.11	7.179	16.58	0.275	634	691	76.70	90.30	13.60	82.3705		80.38		80.18		82.8012		80.81		80.61		95.15		93.16		92.96	
PS 3.5	3.57	11.728	20.17	0.385	583	647	71.80	86.10	14.30	82.1828		80.32		80.06		82.8865		81.03		80.76		103.06		101.20		100.93	
FR DRY	0.02	0.074	18.79	0.164	929	993	78.40	94.80	16.40	90.03	4.23	87.21	4.49	88.04	4.35	90.0359	4.75	87.22	4.76	88.04	4.62	90.16	22.66	87.34	20.52	88.17	21.42
FR 1.6	1.59	5.618	22.90	0.283	756	832	73.90	93.10	19.20	89.84		86.76		87.89		90.1783		87.09		88.23		99.84		96.76		97.89	
FR 2.7	2.69	9.250	25.81	0.385	679	742	71.90	88.10	16.20	88.74		85.70		86.90		89.2926		86.25		87.45		105.20		102.16		103.36	
FR 3.8	3.76	12.597	28.56	0.478	641	695	71.10	85.60	14.50	88.67		85.69		86.88		89.4308		86.44		87.64		111.10		108.11		109.31	
FR 6.3	6.32	19.918	34.36	0.714	599	649	67.10	81.10	14.00	87.76		85.02		86.11		88.9538		86.22		87.31		123.21		120.48		121.57	

Table 2. Summary of results derived from modelling of thermochemical and rheological experimental measurements. Data are divided into compositions used to constrain a common value of A (i.e. Global Fit) and compositions fitted using this optimal A-value (see text). N denotes the number of viscosity experiments. The model values reported include A_{AG} (-3.51), B_{AG}, S^c, and the model calculated values of Tg (K) and fragility (*m*).

		Experimental Measurements			**AG (Global Fit: A_{AG} = -3.51)**			
		H_2O	log η	Cp^c	B_{AG}	S^c	Tg	Fragility
Label	Source[1]	wt. %	N	J mol^{-1} K^{-1}	J mol^{-1}	J mol^{-1} K^{-1}	K	*m*
Used for Global Fit								
ET	TW	0.02	10	21.05	160252	10.7	961	45.9
ET-801-1	TW	0.64	6	21.66	407278	31.7	828	26.1
BET1-3	TW	1.64	6	23.62	271133	22.3	783	31.9
An100	TW	0.00	66	25.29	164228	9.4	1130	57.3
An100H	TW	2.90	4	26.75	213279	16.2	851	41.2
An42Di58H3	TW	2.70	4	25.72	315456	25.6	796	31.1
HAB0	B	0.00	8	4.85	140779	8.8	1032	24.1
HAB2.2	B	1.87	8	10.45	277800	25.2	712	21.9
PHON0	B	0.00	20	11.68	234742	16.6	913	26.4
PHON0.5(B)	B	0.78	11	13.59	221059	17.2	827	27.7
PHON2.2	B	2.15	8	15.67	295090	27.8	684	24.2
TRACH	B	0.00	24	12.79	218516	14.6	963	29.1
TRACH50	B	0.57	9	15.59	240146	17.5	883	29.3
TRACH2.2	B	2.19	9	16.36	328571	28.9	733	24.3
TEPHDRY	B	0.00	22	23.54	172744	12.0	927	45.9
NIQ-0	B	0.00	20	23.36	145785	10.3	916	50.8
NIQ0.6	B	0.68	7	25.66	185250	14.1	849	43.8
DK89	B	0.00	14	8.93	162341	10.6	991	28.6
FR	D	0.0	12	18.08	202952	13.3	981	34.6
FR-1.6	D	1.59	4	24.74	283054	23.4	781	28.3
PS	D	0.0	12	11.16	389039	31.3	800	21.0
PS-0.5	D	0.72	4	12.18	139020	12.6	709	30.4
PS-1.1	D	1.16	4	12.92	184876	17.9	667	26.7
Fitted to A= -3.51								
ET-800-1	TW	1.13	4	24.15	434701	35.3	795	26.1
ET-802-1	TW	2.31	3	25.03	351593	30.5	742	28.2
An90Di10H1	TW	1.53	3	25.48	299677	21.8	885	33.6
An90Di10H2	TW	2.56	4	25.72	339279	26.1	839	30.8
An42Di58H1	TW	1.05	3	25.02	231958	16.9	886	38.5
AN10Di90H2	TW	1.69	3	24.23	194494	15.0	833	40.5
AN10Di90H3	TW	1.75	3	26.42	223778	17.5	823	38.9
An10Di90H4	TW	2.58	3	28.76	204623	16.7	788	42.2
PHON5	B	4.72	3	16.06	220095	23.8	596	26.0
TRACH5	B	4.92	3	17.07	227639	23.4	628	26.8
TEPH1.5	B	1.60	3	27.49	328597	26.0	815	31.9
TEPH2.22	B	2.27	3	32.42	220010	17.9	794	43.6
NIQ1.88	B	1.88	3	33.02	354117	29.7	769	32.8
FR-2.7	D	2.69	5	16.120	194064	17.5	715	29.8
FR-3.8	D	3.76	3	14.490	175261	16.6	681	29.1
FR-6.3	D	6.32	3	14.040	153889	15.5	642	29.6
PS-2.2	D	2.11	3	13.680	221170	22.7	627	24.8
PS-3.5	D	3.55	4	14.280	140296	15.2	597	30.1

[1]Sources include this work (TW) and literature: (B) Bouhifd et al. (2006, 2013); (D) Di Genova et al. (2014).

Appendix A. Modelling Methodology

Our goal is to gain insight into the energetics of the melt to glass transition. Specifically we would like to investigate the configurational entropy associated with the glass transition. Richet and Bottinga (1984) estimate the magnitude of residual configurational entropy at the glass transition temperature (S_c(Tg)) from the calorimetric cycle using enthalpy and heat capacity data available for crystalline material and for the glass and melt counterparts. Toplis et al. (1997) explored another route for estimating S_c(Tg) by combining calorimetric measurements on glasses and melts and measurements of viscosity on the same melts (e.g., Richet and Bottinga, 1995; Richet and Neuville, 1992). The Adam-Gibbs theory provides a robust connection between the transport or relaxation properties of melts (i.e. viscosity) and their thermochemical properties (Adam and Gibbs, 1965; Richet, 1984):

$$Log\,\eta = A + \frac{B}{T\,S^c(T)} \quad . \qquad (A1)$$

Toplis et al. (1997) fit the Adam-Gibbs model to measured values of melt viscosity and estimated values of configurational heat capacity for 3 melt compositions (Table A1) using an expanded form of Eq. A1 where *Sc(Tg)* occurs as an adjustable parameter. This approach has been adopted and modified by a number of other workers (e.g., Toplis, 1998; Webb, 2008; Whittington et al., 2009; Avramov, 2013).

The Data

Here we follow this same approach and apply the method to hydrous melts and glasses. The main difference is that we assume that all silicate melts converge to a single, common, but unknown, value at high temperature. This strategy has a sound theoretical basis, strong empirical support, and creates substantially more reliable estimates of the other adjustable parameters (cf. Russell et al. 2002; 2003; Russell and Giordano, 2005)). The approach is therefore to:

i) synthesize hydrous melts below their solubility limits at high pressure and temperature and quench them isobarically to produce homogeneous unvesiculated hydrous glasses;

ii) use differential scanning calorimetry to measure: the heat capacity of the glass (Cp_g)immediately below Tg (i.e. the onset of Tg) and of the melt (Cp_m) immediately above Tg;

iii) calculate the configurational heat capacity (Cp_c) as Cp_m - Cp_g);

iv) measure the high and low temperature viscosity of the same melt.

These datasets are integrated and used to constrain the Adam-Gibbs equation (Eq. A1) for describing the T-dependent viscosity of melts. The configurational entropy at the temperature of interest (T) is replaced by:

$$S_c(T) \;=\; S_c(Tg) \;+\; \int_{Tg}^{T} \frac{Cp_c}{T}\, dT \qquad (A2)$$

where Cp_c is the configurational heat capacity of the melt-glass transition. Assuming that Cp_c is independent of T, integration of A2 and substitution into A1 provides the expression:

$$log\,\eta \;=\; A \;+\; \frac{B}{T\,[S_c(Tg) \;+\; Cp_c\, ln(^{T}/_{Tg}]} \qquad A3$$

where A, B and $S_c(Tg)$ are adjustable unknown parameters to be solved for by fitting A3 to experimentally measurements of Cp_c, Tg and η.

Optimization Philosophy

Below we demonstrate our approach to fitting the Adam-Gibbs equation to experimental measurements of Tg, Cp_c, and pairs of η:T(K) to obtain estimates of A, B and $S_c(Tg)$ (Eq. A3). We illustrate our philosophy by remodelling the data from Toplis et al. (1997) for Albite (Ab), Jadeite (Jd), and Nepheline (Ne) melts (m=3). Each dataset suggests a system of n non-linear equations for each melt composition of the form:

$$log\,\eta_i \;=\; A \;+\; \frac{B}{T_i\;[S_c(Tg) \;+\; Cp_c\, ln(^{T_i}/_{Tg})\,]} \qquad for\; i = 1{:}n \qquad (A4)$$

where the three adjustable parameters A, B, S_c(Tg) are unique unknowns for each melt composition and n is the number of measured pairs of η:T(K).

As stated above, we have adopted the work of Russell et al. (2002; 2003) and Russell and Giordano (2005) and assumed that silicate melts approach a common high-temperature limiting value (i.e. *A*). This implies a single unknown value of *A* for all melts. Toplis et al. (1997) optimizations of the Ab, Ne and Jd melts also yielded a very narrow range of individual *A*-values (Table A1; -2.38 to -2.53) and on that basis Webb (2008) adopted a single averaged value of *A* (-2.61) from Toplis (1998) for her modelling.

Thus, we have elected to fit Adam-Gibbs equations (Eq. A3) to the calorimetric (Tg, Cp_c) and viscosity datasets for Ab, Jd, Ne melts simultaneously (Table A1). We solve a single system of equations (cf. A4) comprising the m=*3* datasets by minimizing the function:

$$\chi^2_{min}(\boldsymbol{x}) = \sum_{j=1}^{m}\sum_{i=1}^{n_j}\left[\frac{log\,\eta_i - A - B_j/\left(T_i\left[S_{c_j} + Cp_{c_j}\,ln\left(\frac{T_i}{Tg_j}\right)\right]\right)}{\sigma_i}\right]^2 \qquad (A5)$$

where $\boldsymbol{x}$ denotes the solution vector comprising a common value of A, and 2*m* values of B and S_c(Tg), each. There are a total of 36 ($\Sigma_j\, n_i$) observations of viscosity for the *m* melt compositions (Table A1). The objective function is weighted to uncertainties (σ_i) on viscosity arising from experimental measurement.

Covariance Analysis

The form of the Adam-Gibbs function is non-linear with respect to the unknown parameters and, therefore, A5 is solved by conventional iterative methods (*e.g.*, Press *et al.,* 1986). One attribute of using the χ^2 merit function (A5) is that, rather than consider a single solution that coincides with the minimum residuals, we can map a solution region at a specific confidence level (e.g., 1σ; Press et al., 1986). This allows delineation of the full range of parameter values (e.g., A, B_j, and Sc_j) that can be considered equally valid descriptors of the experimental data at the specified confidence level (e.g., Russell et al., 2002). Furthermore, the confidence limits accurately portray the magnitude and nature of covariances between model parameters.

Russell et al. (2002; 2003) showed that the non-linear character of non-Arrhenian models ensures strong numerical correlations between, and even non-unique estimates of, model parameters. One result of the strong covariances between model parameters is that wide ranges of values can be used to describe individual datasets. This is true even where the data are numerous, well-measured, and span a wide range of temperatures and viscosities. Stated another way, there is a substantial range of model values which, when combined in a non-arbitrary way, can accurately reproduce the experimental data.

We illustrate these concepts explicitly by displaying the covariances between parameters for each of the three datasets fitted independently with unique values of A, B and S_c (Fig. A1; Table A1). The 1σ confidence envelopes on the optimal 3 parameter solutions define 3-D ellipsoids; the 2-D ellipses plotted in Figure A1 approximate those confidence envelopes on two parameters where the third parameter is fixed at the optimal solution. These ellipses are planes through the 3-D ellipsoid that contain the solution and are parallel to the fixed parameter. For example, Figure A1 shows the range of values of A and B permitted (and the apparent correlation) fixed at the optimal value of S_c and the magnitude and nature of their covariance. As might be expected given the form of equation A3, the model-induced covariance is strongest between B and S_c. An additional consequence of the model is the negative covariance between A and B *vs.* a positive covariance between A and S_c.

The magnitudes of covariance between adjustable parameters also varies for the individual melt compositions. These variations reflect 3 main elements, in decreeasing order of importance: i) the degree of non-Arrhenian behaviour (i.e. fragility), ii) the temperature-distribution of data, and iii) the quality of the data. Near-Arrhenian melts with low fragility numbers (*cf.* Table A1) allow for wide ranging, but strongly correlated, parameter estiamtes (*cf.* Ab *vs.* Ne; Fig. A1).

Optimization to a Common A

The optimal parameters derived from simultaneous solution of the 3 datasets (Ab, Jd, Ne) assuming a common value of A are summarized in Table A1 and Figure A2. The original viscosity data are reproduced to within experimental uncertainty (Fig. A2, inset). In Figure A2, the 1σ confidence limits on B and S_c are shown for a fixed value of A (i.e. optimal solution A = -3.8). The confidence envelopes are computed by mapping boundaries of constant χ^{2*} around the optimal solution in the manner described fully by Press et al. (1986). The optimal solution is defined by the minimum χ^2_{min} from which a value of $\Delta\chi^{2*}$ (i.e. χ^{2*} - χ^2_{min}) is set; the value of $\Delta\chi^{2*}$ depends on the degrees of freedom and the confidence level of interest.

The matrix $\alpha(2m+1, 2m+1)$ is then calculated for the $\chi^2_{\min}$ fit from

$$\alpha_{k,l} = \sum_{i=1}^{n} \frac{1}{\sigma_i} \left[\frac{\partial y_i}{\partial x_k} \frac{\partial y_i}{\partial x_l} \right] \qquad \text{(A6)}$$

where $\alpha(k,l)$ are the individual entries on the matrix and y_i are the functions (A4) evaluated at the solution. The covariance matrix (C) to the problem is the inverse of α.

We have portrayed the confidence limits as 2-D ellipses resulting from the projection of the solution onto a single plane where the other parameter (A) is fixed at the optimal solution (e.g., Fig. A2). These 2-D ellipses are computed from the matrix equation:

$$\Delta\chi^{2*} = r \cdot \left[C_p\right]^{-1} \cdot r' \qquad \text{(A7)}$$

where C_p is calculated from $[\alpha_p]^{-1}$ and α_p is the 2x2 submatrix of the original matrix α containing rows and columns of the parameters of interest (e.g., $S_{c\,Ab}$ and B_{Ab}). The unknowns to this matrix equation are the two components of the relative displacement vector r (i.e. r_x , r_y or r_{Sc} , r_B). In its quadratic form, equation A7 becomes:

$$r_x^2\, C_p(1,1) + 2\, r_x r_y\, C_p(1,2) + r_y^2\, C_p(2,2) = \Delta\chi^{2*} \qquad \text{(A8)}$$

The coordinates are calculated by fixing one unknown (e.g., r_y) and solving A8 for its roots. Given arbitrary values of r_y, the values of r_x are computed from:

$$r_x = \frac{-r_y\, C_p(1,2) \pm \sqrt{\left(r_y\, C_p(1,2)\right)^2 - C_p(1,1)\left(r_y^2\, C_p(2,2) - \Delta\chi^{2*}\right)}}{C_p(1,1)} \qquad (A9)$$

Operationally we search for coordinate pairs across the minimum and maximum range of values for r_y established by the relationship:

$$r_y = \pm \sqrt{\frac{-C_p(1,1)\, \Delta\chi^{2*}}{C_P^2(1,2) - C_p(1,1)\, C_p(2,2)}} \qquad (A10)$$

Forward Modelling

To the uninitiated, the range of values of B and S_c (Fig. A2) consistent with the experimental dataset (Fig. A2, inset) may be larger than expected. To illustrate and emphasize the consistency of these confidence envelopes with the original viscosity measurements we have calculated families of Adam Gibbs functions (Eq. A3) using the combinations of B and S_c that define the ellipses in Figure A2. The limits to the families of Adam Gibbs functions are denoted in Figure A3 by two dashed lines delineating a shaded field and are compared directly to the original viscosity measurements and to the optimal fit (solid line). The dashed lines are essentially the 1σ confidence limits on the model function.

In all three cases the family of curves derived from the confidence envelopes (Fig. A2) define narrow bands that are entirely consistent with the measurement uncertainties on the original datasets. The experimental data are permissive of a wide range of values of B and S_c, however, the strong correlations between parameters (Fig. A2) control how these values are combined. Thus, even though a wide range of parameter values are considered, they generate a narrow band of Adam Gibbs functions that are entirely consistent with the experimental data.

Compositional Dependence

We conclude this appendix with a comparison of our model values of A, B and S_c to the original work of Toplis et al. (1997). Our single value of A (-3.80) describes the three datasets well but is ~1 log unit lower than the values obtained by Toplis et al. (1997). Our fitting strategy is different in that we use a fixed value of Cp_c (Table A1) taken from his paper whilst they employed a temperature dependent equation. Despite the slight difference in values, Toplis et al. (1997) obtained virtually the same A value for each of their melts supporting our concept of optimizing for a common A.

Our values of S_c are plotted in Figure A4 and agree well with the values estimated by Toplis et al. (1997) and reproduce the overall compositional pattern (e.g., dependence on SiO_2 content). More data would be required to assess whether our slightly higher value for Ne and lower value for Ab are better estimates or not. Our values of B are very close numerically to those of Toplis et al. (1997), however, the relative values for the Ab and Jd melts are switched.

In the case of derivative properties, including Tg and fragility (m), our model returns similar values and similar patterns to those calculated by Toplis et al. (1997) (Table A1). Ne is the most fragile melt (37.6 *vs*. 33.9) and Ab melt is the strongest (26 *vs*. 22.6). The values of *m* obtained by simply fitting each viscosity dataset to a standard temperature dependent equation for non-Arrhenian melts (i.e. the Vogel-Fulcher-Tamman equation; Fulcher, 1925) agree more closely with our values (Ab: 26 vs. 24.2; Jd 28.3 vs. 27.7; Ne: 37.6 vs. 40.2). Estimated of glass transition temperatures (Tg ~ T where $\eta = 10^{12}$ pa s) are also in good agreement with values obtained from modelling the viscosity data by itself (Table A2).